Cholecystokinin-expressing (CCK+) basket cells are key controllers of theta-gamma coupled rhythms in the hippocampus

Alexandra P Chatzikalymniou[1,2†], **Spandan Sengupta**[1], **Jeremie Lefebvre**[1,3‡], **Frances K Skinner**[1,4*‡]

*For correspondence:
frances.skinner@utoronto.ca (FKS)

‡These authors contributed equally to this work

Present address: †Stanford University

[1]Krembil Brain Institute, University Health Network, Toronto, Ontario, Canada;
[2]Department of Physiology, University of Toronto, Toronto, Ontario, Canada;
[3]Department of Biology, University of Ottawa, Ottawa, Ontario, Canada; [4]Departments of Medicine (Neurology) & Physiology, University of Toronto, Toronto, Ontario, Canada

Abstract

Various inhibitory cell types underlie cognitively important brain rhythms and their couplings. Precisely how this is manifest is unclear. Complex network interactions make an understanding of inhibitory cell contributions extremely difficult and using experiments alone is insufficient. Using detailed biophysical models, we obtain hypotheses of how theta and gamma rhythms in the hippocampus are generated and coupled. We find critical contributions by parvalbumin-expressing (PV+) basket cells (BCs), cholecystokinin-expressing (CCK+) BCs and bistratified cells. Based on this, we develop and explore a population rate model and predict that CCK+BCs exert more control relative to PV+BCs for theta-gamma coupling, and that theta frequencies are more strongly affected by PV+BC to CCK+BC coupling relative to CCK+BC to PV+BC. As specific inhibitory cell types can be targeted during behaviour, it is possible to test these predictions. Our work shows that combining models at different scales creates new insights that otherwise would not be revealed.

Introduction

We are now firmly in an era of distinct interneuron or inhibitory cell types, and it is apparent that the different interneuron types need to be considered from functional viewpoints in cognition and behaviour (*Fishell and Kepecs, 2020*; *Kepecs and Fishell, 2014*; *Klausberger and Somogyi, 2008*; *McBain and Fisahn, 2001*). There is a wide range of rhythmic brain frequencies that have been recorded in local field potentials (LFPs) and electroencephalograms (EEGs) arising from dynamic interactions of excitatory and inhibitory cell types in brain circuits (*Buzsáki, 2006*). Moreover, it is becoming clear that cross-frequency coupling (CFC) between high and low frequency rhythms may play functional roles in sensory, motor and cognitive events (*Canolty and Knight, 2010*).

The hippocampus is a heavily studied brain structure that expresses rhythmic activities with well-defined behavioural correlates (*Buzsaki, 2011*; *Colgin, 2016*). In particular, the theta oscillation (≈3-12 Hz) is a prominent LFP rhythm that is most robustly recorded from the CA1 region of the hippocampus (*Buzsáki, 2002*). This rhythm enables multiple timescale organization of neuronal assemblies facilitating the spatio-temporal encoding of events during episodic recall (*Buzsáki and*

40 *Moser, 2013*). Indeed, it has been suggested that 'the single theta cycle is a functional unit capable
41 of representing distinct temporal-spatial content at different phases' (*Wilson et al., 2015*). Interest-
42 ingly, disruptions of hippocampal theta rhythms are associated with memory impairments (*Robbe*
43 *and Buzsáki, 2009*). Higher frequency gamma rhythms ($\approx$ 20-100 Hz) occur nested in these theta
44 oscillations (*Buzsáki et al., 1983*; *Colgin, 2015*), and CFC of these rhythms are considered central to
45 hippocampal function (*Colgin et al., 2009*; *Tort et al., 2008*) with possible causal roles (*Radiske et al.,*
46 *2020*). Dynamic modulation of theta/gamma rhythms during sleep (*Bandarabadi et al., 2019*), vi-
47 sual exploration (*Kragel et al., 2020*) and association with working memory (*Axmacher et al., 2010*;
48 *Lega et al., 2016*) have been documented. It is perhaps not surprising that mounting evidence
49 points to specific changes in theta-gamma coupling with memory impairments, disease and its pro-
50 gression (*Goutagny et al., 2013*; *Hamm et al., 2015*; *Karlsson et al., 2022*; *Kitchigina, 2018*; *Musaeus*
51 *et al., 2020*; *Zhang et al., 2016*).

52 While it has been shown that specific cell types contribute in particular ways to generating theta
53 and gamma rhythms, exactly how they contribute to control these rhythms and how they mutually
54 interact is far from clear. In trying to understand the contributions of specific cell types, it has long
55 been noted that there is a separation between perisomatically and dendritically targeting interneu-
56 ron types onto pyramidal cells (*Freund and Buzsáki, 1996*; *McBain and Fisahn, 2001*). Thus, one can
57 consider a dichotomy in the inhibitory control of pyramidal cell excitability. Further, *Freund* (*2003*)
58 has described another dichotomy of perisomatically targeting cholecystokinin-expressing (CCK+)
59 and parvalbumin-expressing (PV+) basket cells (BCs) in a 'rhythm and mood' fashion (*Freund, 2003*;
60 *Freund and Katona, 2007*), with PV+BCs contributing in a precise clockwork fashion and CCK+BCs in
61 a highly modulatory way. Many mathematical models have been created to help decipher the com-
62 plexity of excitatory and inhibitory interactions underlying theta and gamma rhythms and their cou-
63 plings (*Ferguson and Skinner, 2015*). In particular, circuit models that include explicitly-identified
64 and characterized cell types have been developed (*Bezaire et al., 2016b*; *Ferguson et al., 2017*;
65 *Ecker et al., 2020*).

66 Bezaire and colleagues developed a full-scale model (FSM) of the CA1 hippocampus that ex-
67 hibits theta and gamma rhythms (*Bezaire et al., 2016b*). This is a biophysically detailed microcir-
68 cuit model with 338,740 cells that includes pyramidal (PYR) cells, PV+BCs, axo-axonic cells (AACs),
69 bistratified cells (BiCs), CCK+BCs, Schaeffer Collateral-associated (SCA) cells, oriens lacunosum-
70 moleculare (OLM) cells, neurogliaform (NGF) cells, and ivy cells. The FSM provides a realistic repre-
71 sentation of the hippocampus which is grounded upon a previously compiled, extensive quantita-
72 tive analysis (*Bezaire and Soltesz, 2013*). The authors used their FSM to shed light on the generation
73 mechanism of theta rhythms by describing the activities of the nine cell types. In broad terms, the
74 FSM distinguished the importance of certain cell types against others, and predicted that cell type
75 variability is necessary for theta rhythms to occur.

76 The very complexity of the FSM poses a challenge in the elucidation of explicit mechanisms
77 producing theta rhythms and theta-gamma coupling from an inhibitory cell type perspective. On
78 the one hand, we very much need cellular-based network models to help us untangle the various
79 facets of the interacting dynamics of the network system that produces theta and gamma rhythms
80 and their coupling as this cannot come from experiments alone. Simply identifying and targeting
81 the many different inhibitory cell types during ongoing behaviours and rhythmic activities is an
82 immense, ongoing experimental challenge that is extremely laborious (*Dudok et al., 2021a*,b; *Leão*
83 *et al., 2012*). On the other hand, the presence of nonlinearity, high-dimensionality and degeneracy
84 in detailed models makes it difficult to extract explicit mechanisms.

85 In this paper, we build on our previous work (*Chatzikalymniou et al., 2021*) and take a deep
86 dive into the FSM of *Bezaire et al.* (*2016b*). We leverage these examinations to develop precise hy-
87 potheses of how theta and gamma rhythms are generated, interact with each other, and how the
88 different cell types mediate these interactions. We identify four cell types (PYR cells, PV+BCs, BiCs,
89 CCK+BCs) that are deemed essential, and we confirm this by selective deactivation of their intercon-
90 nections. We build a population rate model (PRM) using these four cell types and find a parameter

91 set that can capture the developed hypotheses. We then do systematic parameter explorations
92 of the PRM to expose dynamic 'balances' underlying the rhythmic expressions in the network sys-
93 tem. We exploit detailed visualizations of the system and predict that CCK+BCs exhibit a much
94 higher degree of control relative to PV+BCs for the dominance of either theta or gamma rhythms
95 in the network system, and thus theta-gamma coupling. Given that it is possible to specifically tar-
96 get PV+BCs and CCK+BCs in the behaving animal (*Dudok et al., 2021a*), this prediction opens up a
97 plethora of possibilities that can be experimentally examined. Moreover, our work shows that de-
98 veloping, analyzing and combining mathematical model types at different scales and abstraction
99 brings about insights that would not be possible if only one model type were used. Interestingly,
100 model diversity has recently been noted as needed to be able to have an immense impact on our
101 understanding of the brain (*Eriksson et al., 2022*).

Results

103 To have a starting basis for examinations using the FSM, we reproduced theta-gamma rhythmic
104 output in the FSM of *Bezaire et al.* (*2016b*). This is shown in FIGURE 1. In FIGURE 1A, we present
105 a stylized schematic of the nine different cell types in the FSM. Connections between the different
106 cell types are represented by grey lines between them. Grey circles by a given cell type indicates
107 that they are interconnected, and incoming grey lines to the different cell types represent external
108 drives. The thickness of the lines and circles is representative of the relative strength of these
109 various connections. They reflect computed effective weights (EWs) and external drives in the FSM.
110 The specific values are given in the Methods (see TABLE 1 for drives, and TABLES 2-3 for EWs). The
111 raw unfiltered LFP output from the network model is shown in FIGURE 1B(i) with its power spectra
112 in FIGURE 1B(ii). The raster plot output for each of the nine cell types is given in FIGURE 1C(i) for 4
113 seconds. As has been shown experimentally, these rhythms can be generated intra-hippocampally
114 and do not require the medial septum (MS) (*Goutagny et al., 2009*; *Jackson et al., 2011*). This does
115 not mean that the MS is not important for theta rhythms, rather, it implies that the expression of
116 these rhythms does not have explicit reliance on the MS and can be generated by hippocampal
117 circuitry on its own.

Anatomy of a theta cycle in the full-scale model (FSM)

119 *Bezaire et al.* (*2016b*) identified a number of model properties as important for theta rhythms. They
120 showed that diverse inhibitory cell types and the existence of recurrent excitation are necessary
121 for the presence of these rhythms. They also performed mutation simulations and identified the
122 cell types that were necessary for the rhythm versus those that could be removed without having
123 much of an effect. Specifically SCA, OLM and ivy cell types were found to not be necessary. On the
124 other hand, BiCs, PV+BCs and PYR cells were necessary and further, these cell types are strongly
125 theta modulated (see Figure 5A in *Bezaire et al.* (*2016b*), and we quantify this modulation in more
126 detail in FIGURE 1-Supplement 1. The remaining cell types are CCK+BCs, AACs and NGF cells.
127 To further distill the essence of cell types that would be sufficient to have theta rhythms in the
128 FSM, we examined external drives and connections between all of the cell types given their num-
129 bers and synaptic weights, where computed EWs are representative of cell numbers and synaptic
130 weights (see Methods). Based on this examination, we noted that the AACs have the lowest external
131 drive (not including OLM cells which have zero external drive), and that the NGF cells have either
132 zero or minimal (EWs<1) inputs to them. This can also be easily discerned from the schematic
133 of FIGURE 1 where connection strengths are visualized in a relative fashion. Given this, we con-
134 sidered that PYR cells, PV+BCs, BiCs and CCK+BCs are the critical cell types for the existence of
135 theta rhythms. Focusing on these four cell types, we now move on to develop precise hypothe-
136 ses of theta-gamma rhythm generation in the FSM. Given the high level of biophysical detail in
137 the FSM, it is reasonable to consider it as a biological proxy. Thus, one can consider extrapolating
138 any determined insights of understanding theta-gamma rhythms and couplings to the biological
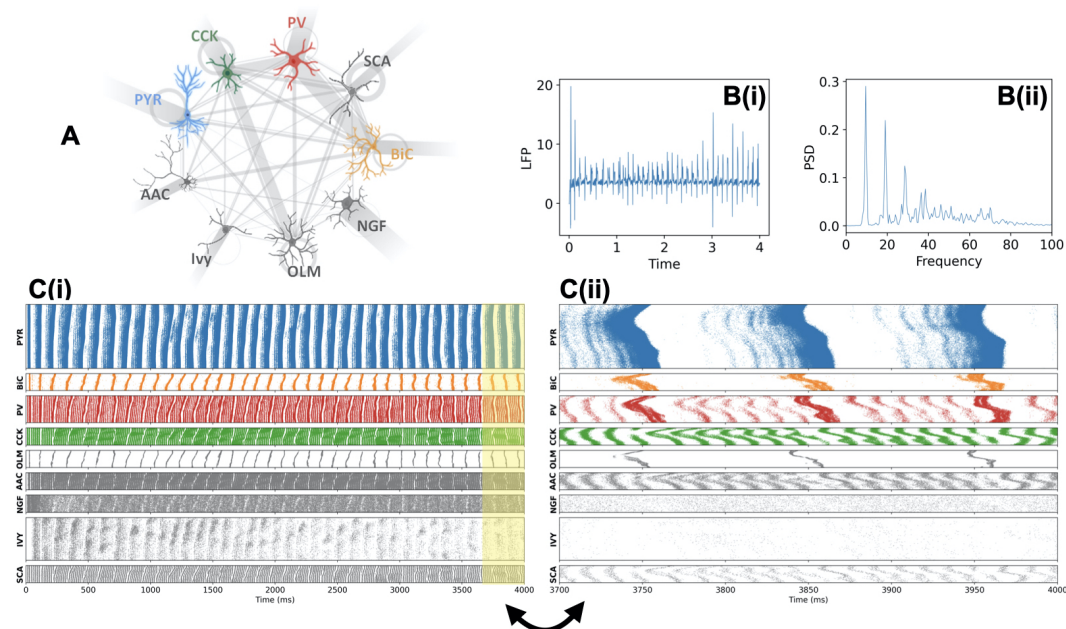139 hippocampal system.

Figure 1. Output of the original full-scale model (FSM).
A. Stylized schematic of the 9 different cell types that are present in the FSM. These cell types are pyramidal (PYR) cells, paravalbumin-expressing basket cells (PV+BCs), axo-axonic cells (AACs), bistratified cells (BiCs), cholecystokinin-expressing (CCK+) BCs, Schaeffer Collateral-associated (SCA) cells, oriens-lacunosum-moleculare (OLM) cells, neurogliaform (NGF) cells, and ivy cells. In the figure, they are referred to as PYR, PV, AAC, BiC, CCK, SCA, OLM, NGF, Ivy, respectively. Connectivities are represented by grey lines - see text for details. **B(i)** unfiltered LFP output (units of mV). **B(ii)** PSD (power spectral density) of LFP (units of mV^2/Hz). **C(i)** 4 second (s) raster plot. **C(ii)** 300 millisecond (ms) raster plot, as taken from the last 300 ms of the simulation. Raster plots are of the excitatory cell types (PYR) and the eight inhibitory cell types (BiC, PV, CCK, OLM, AAC, NGF, IVY, SCA) as in the original CA1 FSM that includes 311,500 PYR (in blue); 2,210 BiC (in orange); 5,530 PV (in red); 3,600 CCK (in green); 1,640 OLM (in grey); 1,470 AAC (in grey); 3,580 NGF (in grey); 8,810 IVY (in grey) and 400 SCA (in grey). The colours match those of the stylized cells in the schematic of **A**.
Figure 1—figure supplement 1. Theta phase preference detail.

140   We now zoom in on 300 msec of the full 4 sec raster plot output to do a careful examination
141 of the cell firings in the FSM. This is shown in FIGURE 1C(ii) where only a handful of theta cycles
142 are present and gamma firings can be discerned. We observe certain dynamics that speak to par-
143 ticularly important connections between the four cell types. At the beginning of any given theta
144 cycle the PYR cells start firing as a result of (noisy) external excitation they receive to initiate the
145 theta rhythm. By virtue of their recurrent connectivity, more and more cells can participate and
146 the PYR cell activity (i.e., the number of PYR cells that are active) is elevated due to the progressive
147 recruitment of PYR cells. This activity increase is easily seen in the PYR cell raster plot (FIGURE 1C(ii)).
148 We already know from our previous modeling work that theta rhythm expression is possible with
149 a large enough number PYR cells that have some recurrent connectivity (*Chatzikalymniou et al.,*
150 *2021*). In that work, we distinguished the PYR cell population, and not any of the inhibitory cell
151 populations, as the theta rhythm initiators. Further, we showed the promotion of increased PYR
152 cell clustering as the recurrent excitation increased (see Figure 6 in *Chatzikalymniou et al.* (*2021*)).
153   Continuing on, we see that at some critical point the PYR cell activity exceeds a certain threshold
154 that leads to significant activation of the BiCs as well as concurrent enhancement of the PV+BC
155 activity. The strong activation of these PV+ cell types (i.e., PV+BCs and BiCs) in turn strongly inhibits
156 the PYR cells, effectively silencing them. That is, the activity of the PYR cells is sharply terminated
157 once it reaches a threshold due to concurrent PV+ cell activation. Once the PYR cell activity drops,
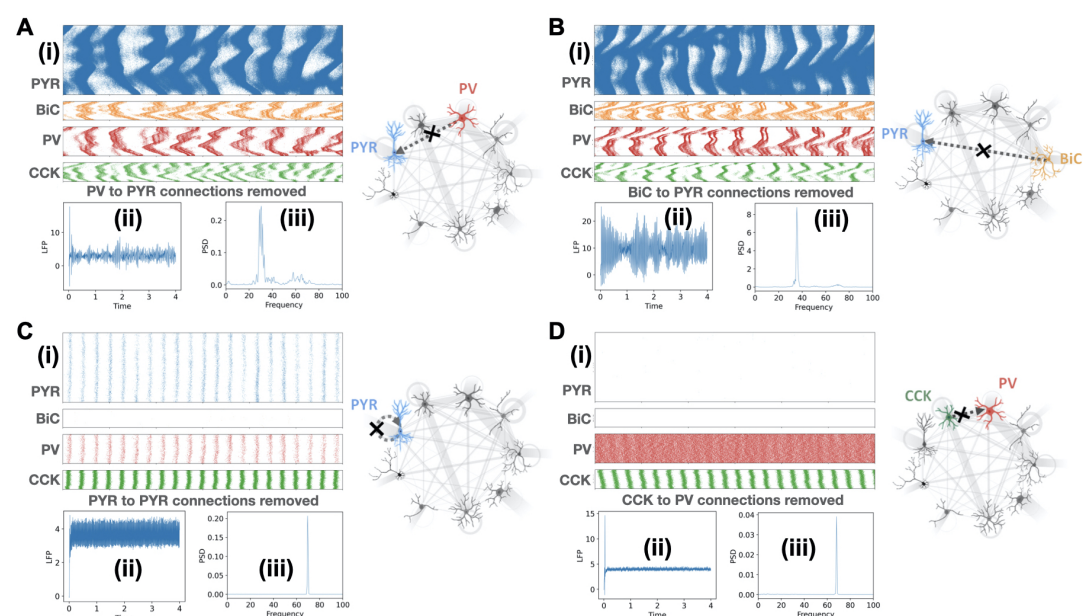158 so does the PV+ cell activity which then eventually leads to the PYR cells being able to start firing

Figure 2. FSM output when connections between different cell types are removed.
A. PV to PYR connections removed. **B.** BiC to PYR connections removed. **C.** PYR to PYR connections removed.
D. CCK to PV connections removed. Each part shows a schematic illustration that highlights the particular connections that are removed, and **(i)** show the last 300 ms of raster plot firings for PYR, BiC, PV and CCK cells.
(ii) unfiltered LFP. **(iii)** PSD of LFP. Units, colors and naming abbreviations are the same as FIGURE 1;
Figure 2—figure supplement 1. Additional connection removals in the detailed model.

159 again. For this, enough PYR cells need to be sitting near their firing threshold. We now evaluate
160 these observations by selectively deactivating connections in the FSM.

Dissecting the theta/gamma FSM circuit

162 We test the sharp theta termination directly by removing either PV+BC or BiC connections to the
163 PYR cells. In FIGURE 2A & B, we show that these removals abolish theta rhythms. That is, the theta
164 bursts simply can't be terminated as the inhibitory connections from PV+BCs or BiCs are no longer
165 there. In FIGURE 2-Supplement 1, we show that theta rhythms are also abolished if the connec-
166 tions from PYR cells to either PV+BCs or BiCs are removed. This is because in the absence of these
167 connections, the PYR cells can't activate these PV+ cells (BiCs or BCs) once they exceed a critical
168 threshold of activity and as a result the PV+ cells can't silence them back to sharply terminate their
169 activity and allow another (theta) cycle to begin. With these connection removals, the PYR cells only
170 exhibit a gamma rhythm due to being entrained by the gamma firing inhibitory cells. We note that
171 these simulations in which we removed particular connections expose different aspects relative to
172 the muting experiments done by *Bezare et al.* (*2016b*). In Bezaire's case, muting the cells essen-
173 tially removed the particular cells from the overall circuit. Here, in removing particular connections,
174 we show the contribution of specific cellular pathways in the generation of theta rhythms.

175   As already noted above, the initiation of the theta rhythm is known to be due to the PYR cell
176 population (*Chatzikalymniou et al., 2021*). The requirement of recurrent connectivity is shown in
177 FIGURE 2C where connections between PYR cells are removed to reveal the loss of theta rhythms.
178 The inhibitory cells contribute to the net input that the PYR cells receive but are not directly re-
179 sponsible for the initiation of the theta rhythm. If there is a reduction in the net input received by
180 the PYR cells and/or the PYR cells are less excitable, then theta rhythms would not be able to be
181 initiated. Interestingly, in our previous modeling we had found that the LFP theta frequency has a
182 linear correlation with the net input received by the PYR cells (*Chatzikalymniou et al., 2021*), and
183 in the FSM of *Bezare et al.* (*2016b*), the particular theta frequency is in line with this correlation.

184 Details are provided in the Methods.

185 Along with PV+BCs and the BiCs, *Bezaire et al.* (*2016b*) showed that CCK+BCs are pivotal for
186 theta rhythms since there is no theta rhythm with the muting of this cell type. In the FSM there are
187 connections from CCK+BCs to PV+BCs, BiCs and PYR cells. Removing connections from CCK+BCs
188 to BiCs does not eliminate the theta rhythm, but the rhythm is lost if connections from CCK+BCs
189 to either PYR cells or PV+BCs are removed. CCK+BCs provide significant amount of inhibition to
190 the PYR cells and thus removing those connections makes the PYR cells hyper-excitable leading
191 to loss of theta (results not shown). However, the loss of theta with the connection removal to
192 PV+BCs is not so intuitive. We were able to probe this thoroughly by using a 'clamped' version of
193 the detailed model network. We did this with a 'slice' of the FSM as used before by *Chatzikalymniou*
194 *et al.* (*2021*). We performed a grid search of each of the postsynaptic weights received by PV+BCs
195 from the different cell types to find out how these weights impact the PV+BC activity. In particular,
196 we found that a small increase in the synaptic weight from CCK+BCs to PV+BCs could lead to a
197 large decrease in PV+BC firing, akin to a 'bifurcation point' in dynamical systems parlance. This was
198 not observed with changes in any of the other synaptic weights from other cell types examined.
199 Details are provided in the Methods. These observations indicate that a strong disinhibition of the
200 PV+BCs, specifically mediated by the CCK+BCs, can induce a sudden increase in the PV+BC firing
201 rate. As shown in FIGURE 2D, this is borne out in the FSM which shows that without CCK+BC to
202 PV+BC connections, there is a large increase in the PV+BC firing rate which in turn shuts down the
203 PYR cells and abolishes theta rhythms. This indicates that CCK+BCs are prominent controllers of
204 PV+BC activity and via that pathway influence theta power.

205 Looking at the zoomed in raster plots of the focused four cell types in FIGURE 1C(ii), one can
206 clearly discern higher frequency gamma rhythms expressed in PV+BCs and CCK+BC+ as well as
207 in the PYR cells where the slower frequency theta rhythms are also apparent. Theta and gamma
208 rhythms are both present in the LFP signal as seen from the power spectrum (FIGURE 1B(ii)). The
209 gamma rhythm seen in the LFP output is produced by the gamma-paced entrainment of the noisy-
210 firing PYR cells as follows: The PV+BCs and the CCK+BCs fire at gamma frequencies and organize
211 themselves into coherently firing populations. The PV+BCs and the CCK+BCs also form connections
212 with the PYR cells. As a result, during a theta cycle these gamma-firing cells periodically inhibit the
213 noisy firing PYR cells forcing them to burst in a gamma-paced manner. This results in a gamma
214 rhythm being present with the progressive recruitment of PYR cells toward the peak of the theta
215 cycle. Because the amplitude of the gamma LFP maximizes at peak of the PYR cell theta burst
216 (which corresponds to the peak of the theta cycle), the amplitude of the gamma rhythm is coupled
217 with the phase of theta, giving rise to phase-amplitude coupling of the theta and gamma rhythms.

A reduced circuit model

219 From the FSM simulations and analyses described above we now have precise cell-based hypothe-
220 ses of how theta/gamma rhythms are generated in the CA1 hippocampus. Namely, the theta
221 rhythm is initiated by the PYR cell population, sharply terminated by PV+BCs and BiCs, and con-
222 nections from CCK+BCs to PV+BCs are essential for theta rhythms. By removing particular con-
223 nections in the FSM, these hypotheses were tested and confirmed. Given this, we feel confident
224 to consider a reduced circuit model that is derivative of the FSM. This reduced model consists of
225 the four different cell types and only those connections deemed essential in light of the developed
226 hypotheses. A schematic of this reduced circuit model relative to the FSM is shown in FIGURE 3.
227 This reduced circuit model motivates the creation of a population rate model (PRM).

Population rate model (PRM) reproduces FSM derived hypotheses

229 Considering the reduced circuit model shown in FIGURE 3, we set up a population rate model
230 (PRM) that is able to exhibit multi-modal (theta/gamma) oscillations. The equations are provided
231 in the Methods. Using this PRM we found a set of parameter values that give rise to theta-gamma
232 rhythms as shown in FIGURE 4A. We refer to these parameter values as 'reference parameters', and
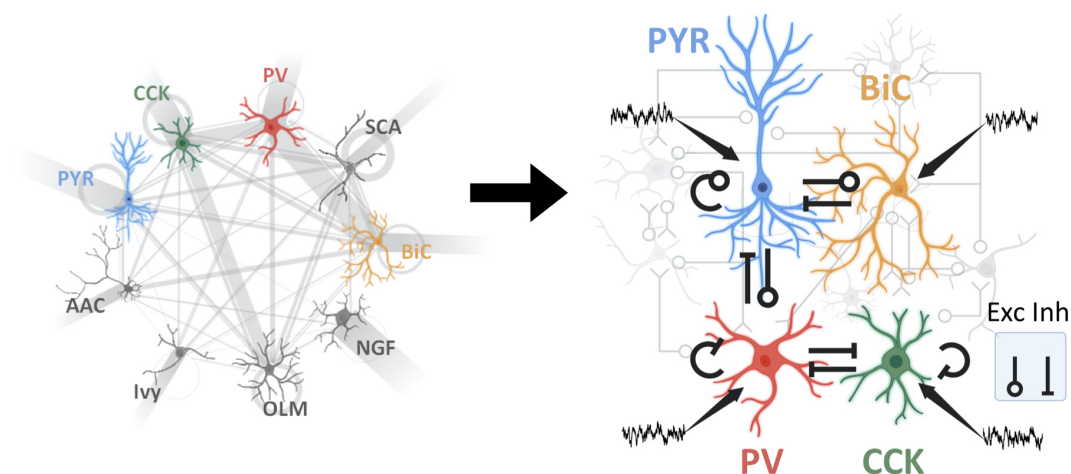
Figure 3. Rationalized reduction in complexity of CA1 hippocampus model circuit.
The left side shows the stylized schematic of the FSM. Detailed descriptions of color and naming abbreviations are given in FIGURE 1. The right side shows a stylized schematic of the reduced model with 4 cell types and excitatory (Exc) and inhibitory (Inh) connections between them and inputs (incoming arrows). The rationale used to consider this reduced model is given in the main text.

233 the values are provided in the Methods (TABLE 4). These theta-gamma rhythms are in accordance
234 with the developed hypotheses. That is, the presence of theta rhythms requires PV+BC and BiC to
235 PYR cell connections as well as CCK+BC to PV+BC connections. In line with the hypotheses, theta
236 rhythms are lost when these various connections are removed, as in FIGURE 4B-D. It is interesting
237 that this reference parameter set produces activities of CCK+BCs and PV+BCs that fire alternately as
238 has been experimentally shown (*Dudok et al., 2021a*). We now undertake a full-blown parameter
239 exploration of the PRM and perform analyses and visualizations of thousands of simulations to
240 obtain the following insights and predictions.

241 PRM predictions are in agreement with FSM predictions on theta frequency control
242 and the requirement of recurrent collaterals

243 In our previous work we showed that the LFP population theta frequency is correlated with the
244 net input received by the PYR cells (*Chatzikalymniou et al., 2021*). Further, this correlation was
245 found to be mostly due to the excitatory external drive and the inhibitory input, and not mainly
246 due to recurrent collateral inputs - see Figure 7d(i-iii) in *Chatzikalymniou et al.* (*2021*). We found
247 that as excitatory or inhibitory input to PYR cells increased, the theta frequency increased. The
248 2-D heat maps of FIGURE 5 show that this is also the case with the PRM. Specifically, increasing
249 the excitatory input to PYR cells (i_{PYR}) led to increases in the theta frequency as shown in FIG-
250 URE 5A(i) where i_{PYR} varies along the x-axis. Increasing the inhibitory input in the form of larger
251 connection weights (i.e., more negative values) from BiCs ($w_{BiC \to PYR}$) or from PV+BCs ($w_{PV \to PYR}$) to
252 the PYR cells also resulted in theta frequency increases. This is shown in FIGURE 5B(i) & C(i) where
253 $w_{PV \to PYR}$ and $w_{BiC \to PYR}$, respectively, vary along the x-axis of the 2-D heat maps. However, modulat-
254 ing the recurrent excitation ($w_{PYR \to PYR}$) did not produce changes in theta frequencies. To show this
255 more directly, we plot theta frequency versus the different parameters in 1-D plots in FIGURE 5A(ii).
256 This plot shows that there is no change in the theta frequency as the recurrent excitatory weight
257 ($w_{PYR \to PYR}$) is changed (blue triangles), but that there is a frequency increase as the excitatory drive
258 i_{PYR} is increased (red circles). Additional plots in FIGURE 5B(ii) & C(ii) show that as inhibitory input to
259 the PYR cells increases, due to either increasing synaptic weights from BiCs ($w_{BiC \to PYR}$) (blue circles
260 in C(ii)) or from PV+BCs ($w_{PV \to PYR}$) (green circles in B(ii)), the theta frequency increases. The partic-
261 ular values shown in these plots are shown as horizontal or vertical lines (red part of the lines) in
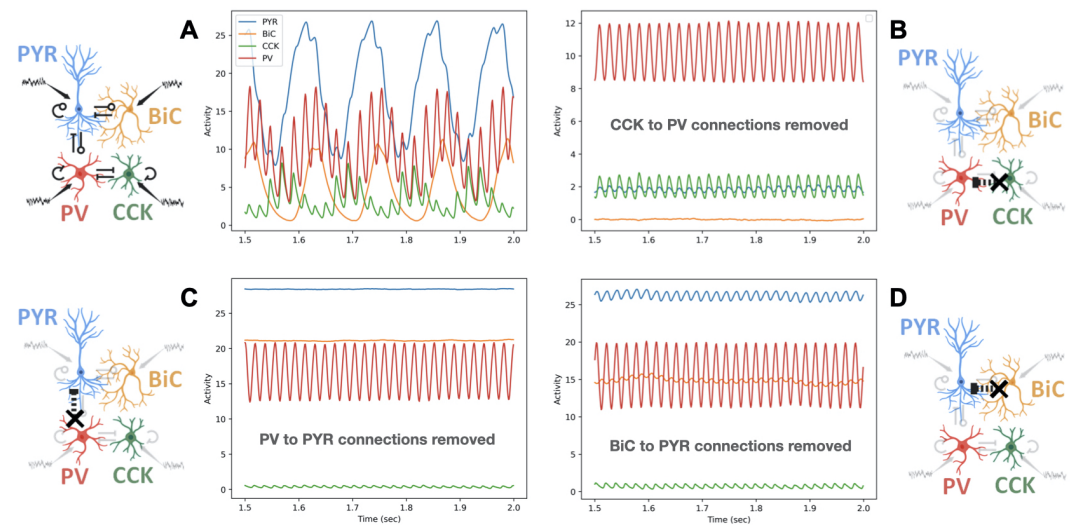
Figure 4. Output of the reduced population rate model (PRM).
A. PRM output of the activity of each cell type population (see TABLE 4 for parameter values). **B.** PRM output when CCK to PV connections are removed. **C.** PRM output when PV to PYR connections are removed. **D.** PRM output when BiC to PYR connections are removed. Naming and color scheme of the 4 cell types is the same as in FIGURE 1. Each part shows a schematic illustration that highlights the particular connections that are removed.

262   the 2-D heat maps of FIGURE 5A(i), B(i) & C(i).

263   Given the different and reduced structure of the PRM, we do not expect a direct correspon-
264   dence between PRM and FSM-generated frequencies. However, it is reassuring that we obtain
265   similar relationships - that is, increases or decreases in theta frequency as previously predicted
266   using the detailed model (*Chatzikalymniou et al., 2021*). This implies that usage of this PRM can
267   produce valid relationships relative to the biological system as represented by the detailed model.
268   We do note that there is much richness in the PRM that can be exposed due to the expansive ex-
269   ploration made possible by its much reduced nature relative to the detailed model. For example,
270   there are parameter regimes in which the theta frequency decreases (rather than increases) when
271   $w_{PV \to PYR}$ connection weights are increased - specifically, for the lower weight (less negative) values
272   of $w_{PV \to PYR}$. This can be seen in the particular heat map of FIGURE 5B(i). In FIGURE 5-Supplement 1,
273   we show the heat maps of theta frequency for the other three cell types (PV+BCs, BiCs, CCK-BCs).

274   As was previously shown (*Bezaire et al., 2016b*; *Chatzikalymniou et al., 2021*; *Ferguson et al.,*
275   *2017*), recurrent connections ($w_{PYR \to PYR}$) are needed for the existence of theta rhythms. To visual-
276   ize this, we compute 2-D difference heat maps that represent the subtraction of the normalized
277   gamma power from the normalized theta power. Blue is used to show where theta rhythms domi-
278   nate, and red where gamma rhythms do. See Methods for details regarding these computations. In
279   this way, we are able to nicely visualize how different parameters affect theta and gamma rhythms
280   and their coupling. In FIGURE 5-Supplement 2, we show difference heat maps for a wide range
281   of $i_{PYR} - w_{PYR \to PYR}$ parameter values, and from it, it is abundantly clear that a non-zero value of
282   $w_{PYR \to PYR}$ is needed to have theta rhythms. In FIGURE 5-Supplement 2, we also show a plot of the
283   activities of the four different cell types when there is no recurrent excitation - theta rhythms are
284   not present.

PRM predicts stronger control by CCK+BCs relative to PV+BCs for theta vs gamma
rhythm dominance

287   In FIGURE 6A & B, we respectively show 2-D difference heat maps of $i_{CCK} - i_{PV}$ and $w_{PV \to CCK} -$
288   $w_{CCK \to PV}$ parameter sets. FIGURE 6A(i) & B(i) maps show parameter ranges that were chosen to
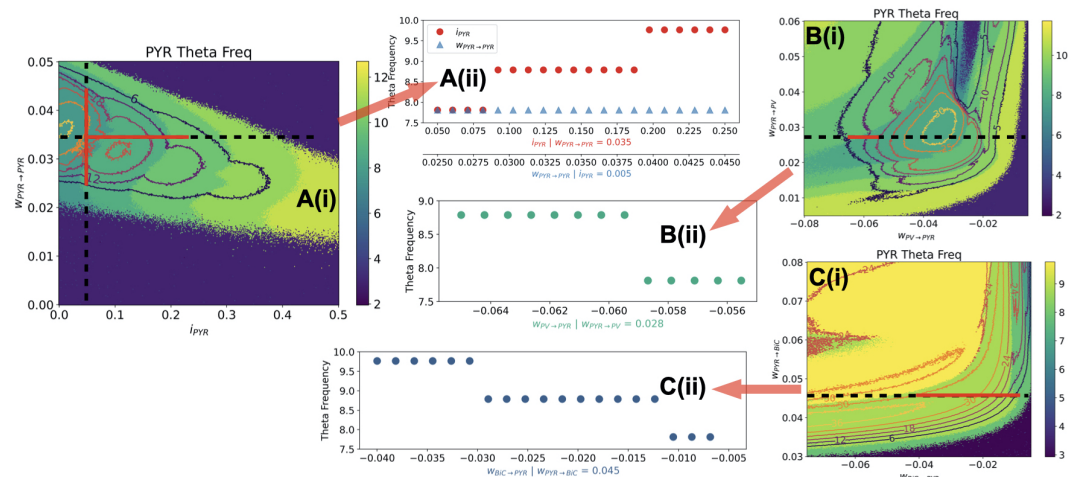
Figure 5. Theta Frequency Control in PRM.
Theta frequency changes in the PYR cells for changes in parameter set pairs. **A.** Heat map for $(i_{PYR} - w_{PYR \to PYR})$ is shown in **(i)** and a plot from a slice is shown in **(ii)**. **B.** Heat map for $(w_{PV \to PYR} - w_{PYR \to PV})$ is shown in **(i)** and a plot from a slice is shown in **(ii)**. **C** Heat map for $(w_{BiC \to PYR} - w_{PYR \to BiC})$ is shown in **(i)** and a plot from a slice is shown in **(ii)**. The contours in the heat maps encompass the 6 highest power values, i.e., where there are high activity values at theta frequencies. 'Slices' of the heat maps are from the indicated dashed black lines, and the plots are specifically shown for ranges indicated by the red part of the dashed black lines, as chosen to more easily see the trends in theta frequency changes.

Figure 5—figure supplement 1. Theta frequency heat maps for other cell types.

Figure 5—figure supplement 2. Difference heat maps.

---

289   clearly show regimes of theta (blue) or gamma (red) rhythm dominance, whereas FIGURE 6A(ii) &
290   B(ii) maps show parameter ranges that are the same for both x- and y-axes. Between the blue
291   and red regions is a yellow region where both theta and gamma rhythms are present - i.e., theta-
292   gamma coupling exists. This theta-gamma coupling is easily seen in the activities of the four cell
293   types in FIGURE 4A for the reference parameters. In particular, in the PYR cell (blue) activity, but
294   also in the PV+BC (red) and CCK+BC (green) activities. To more easily visualize this coupling regime,
295   we add a black line to the difference heat maps of FIGURE 6A & B where switching between gamma
296   or theta dominance would occur, that is, where there is theta-gamma coupling. What is abundantly
297   clear from the steepness of the black lines in these difference heat maps is that CCK+BCs relative
298   to PV+BCs can more strongly control the level of theta versus gamma rhythm dominance. For
299   example, a small change in the amount of input being received by CCK+BCs from PV+BCs ($w_{PV \to CCK}$
300   in FIGURE 6B(i),B(ii)) can switch the dominance of whether theta or gamma rhythms are expressed.
301   This would not be the case for a similar small change in the amount of input being received by
302   PV+BCs from CCK+BCs ($w_{CCK \to PV}$). This stronger control of theta-gamma coupling by CCK+BCs
303   relative to PV+BCs is less obvious in the difference heat maps when the drive to either CCK+BCs
304   (i_{CCK}) or PV+BCs (i_{PV}) (FIGURE 6A(ii)) is considered for the same parameter values. That is, the slope
305   of the black line on the i_{CCK} versus i_{PV} difference heat map (FIGURE 6A(ii)) is less steep than that
306   of the black line on the $w_{PV \to CCK}$ versus $w_{CCK \to PV}$ difference heat map (FIGURE 6B(ii)). In FIGURE 6-
307   Supplement 1, we show the difference maps of theta frequency from the perspective of the other
308   three cell types (PV+BCs, BiCs, CCK-BCs). Difference heat maps with PYR and PV+BC couplings
309   further support this as additional 'input' received by PV+BCs from PYR cells does not sensitively
310   (i.e., steeply) affect theta-gamma coupling - see FIGURE 6-Supplement 2. Overall, it is clear that the
311   CCK+BCs more strongly control theta-gamma coupling relative to the PV+BCs as observed from
312   the different effects of input changes to CCK+BCs or PV+BCs.
313   An interesting observation is that the theta frequency is more strongly affected by modulat-
314   ing connection strengths from PV+BCs to CCK+BCs than the other way. This is visualized in the
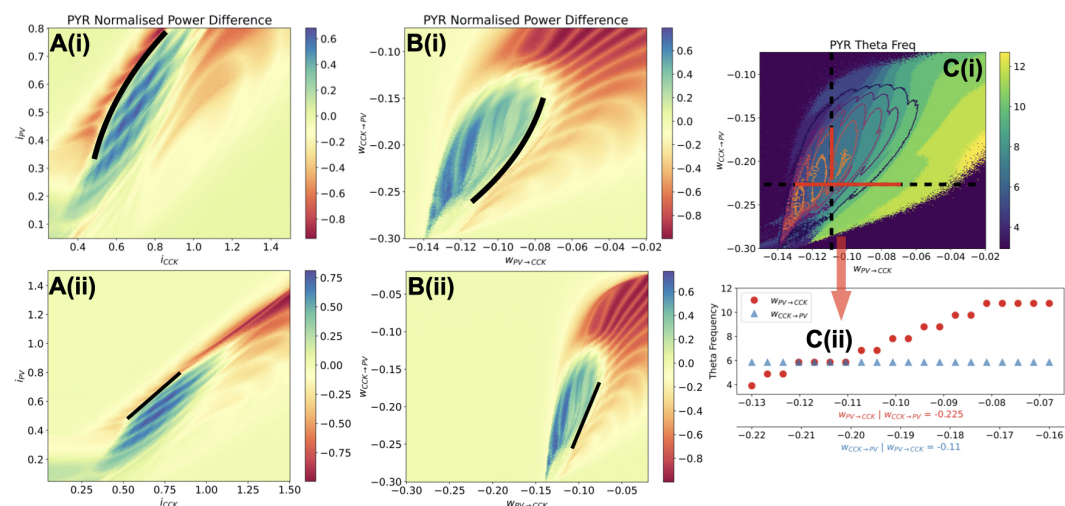
Figure 6. CCK+BCs more strongly control rhythm expression and theta frequencies.
Difference Maps: [(Normalized power of theta) - (Normalized power of gamma)] are shown in **A** and **B**. Positive (blue) values mean that theta rhythms are dominant, and negative (red) values mean that gamma rhythms are dominant. 'Yellow' values mean that theta and gamma powers are comparable so that there is theta-gamma coupling (or that both theta and gamma powers are very small). The difference map plots show CCK+BCs and PV+BCs from drive **A(i)** and connection perspectives **B(i)**, and when viewed for the same parameter range values **A(ii)** and **B(ii)**. Black lines are added to delineate theta and gamma dominant regions. Given the angle of these lines, it is clear that CCK+BCs have a higher level of control relative to PV+BCs in determining whether theta or gamma rhythms are dominant, and hence coupled, since the slopes are steeper for changes from CCK+BC perspectives. **C(i)** shows the theta frequency heat map for $w_{PV \to CCK} - w_{CCK \to PV}$ connection weights and a plot of the theta frequency to show that PV+BC to CCK+BC connection more strongly affect the theta frequency is shown in **C(ii)**. As in Figure 5, the dashed black lines show the 'slices' taken from the heat map in plotting the theta frequency versus either $w_{PV \to CCK}$ (red dots) or $w_{CCK \to PV}$ (blue tranges) for ranges indicated by the red part of the dashed black lines.

Figure 6—figure supplement 1. Additional difference heat maps.

Figure 6—figure supplement 2. Difference heat maps for PYR-PV+BC and PYR-BiC couplings.

frequency heat map shown in FIGURE 6C(i). Similar to FIGURE 5, we show a theta frequency plot (FIGURE 6C(ii))) as these connections are varied, with horizontal or vertical dashed line representing the particular values in the plot where $w_{PV \to CCK}$ (horizontal) or $w_{CCK \to PV}$ (vertical) changes occur. It is clear that the theta frequency minimally changes with $w_{CCK \to PV}$ modulation, unlike with $w_{PV \to CCK}$ modulation. In FIGURE 6-Supplement 1SUPP FIG 4, we show the heat maps of theta frequency for the other three cell types (PV+BCs, BiCs, CCK-BCs).

The prediction of the importance of CCK+BCs for theta-gamma coupling from the PRM was possible because of the extensive and systematic parameter exploration that could be carried out in the reduced circuit model (FIGURE 3). We note that this importance of CCK+BCs in population rhythms is in line with observations from our detailed model explorations described above, but from a different perspective. We had showed that CCK+BCs, unlike any of the other cell types, could drastically affect PV+BC firing which in turn strongly suggests that they underlie the control of theta expression. Indeed, we showed that theta rhythms are not present when CCK+BC to PV+BC connections are removed in the FSM (see FIGURE 2D). Experimentally, CCK+BCs and PV+BCs show complementary activities and CCK+BCs inversely scale with PYR cell activities *Dudok et al.* (*2021a*) This would be in line with disinhibition of PV+BCs by CCK+BCs and its subsequent effect on PYR cell firing. Additionally, *Fasano et al.* (*2017*) have shown that CCK+BCs, as identified by atypical vesicular glutamate transporters, alter theta oscillations.

Discussion

333
334 In this paper, we presented a detailed explanation of how theta and gamma rhythm mechanisms
335 could arise in the CA1 hippocampus and showed that CCK+BCs play a controlling role in theta-
336 gamma coupled rhythms. We built upon earlier modeling studies that brought together minimal
337 (*Ferguson et al., 2017*) and detailed (*Bezaire et al., 2016b*) CA1 microcircuit models with defined
338 inhibitory cell types that produce theta rhythms and showed that large enough PYR cell networks
339 could initiate theta rhythms with inhibitory cell populations 'regularizing' the rhythm. We termed
340 this an 'inhibition-based tuning' mechanism (*Chatzikalymniou et al., 2021*; *Skinner et al., 2021*). The
341 theta rhythm generation is initiated by the PYR cell population which also sets the theta frequency,
342 but the termination of the theta bursts is an inhibition-mediated mechanism which contributes to
343 the robustness and stability of the rhythm. In their original study, *Bezaire et al.* (*2016b*) described
344 the preferential discharge of the PYR cells at the trough of the LFP analog and the subsequent
345 strong recruitment of PV+BCs and BiCs to silence the PYR cells, but the specifics leading to the ter-
346 mination of the theta burst were not parsed out. They also described the progressive recruitment
347 of PYR cell firings towards the peak of the theta cycle, but the prominent role of the PYR cells as
348 theta rhythms initiators was first demonstrated and discussed in *Chatzikalymniou et al.* (*2021*).

349 From our explorations of the detailed model here, we directly showed that PV+BCs and BiCs
350 are responsible for the sharp termination of PYR cell firing. Of note, we found that CCK+BCs, more
351 than any other inhibitory cell type, play a key role in PV+BC firing. Gamma rhythms arose due to
352 coherent firing in CCK+ and PV+ basket cell networks. Using the four cell types of PYR cells, PV+BCs,
353 CCK+BCs and BiCs, we generated theta-gamma rhythms in a reduced population rate model (PRM).
354 The PRM reproduced the specific contributions of these four different cell populations seen in the
355 detailed full-scale model (FSM). From extensive simulations and visualization analyses of the PRM,
356 we predicted that CCK+BCs more strongly controlled theta-gamma coupled rhythms than PV+BCs.
357 We further predicted that PV+BC to CCK+BC connections can more strongly affect theta frequencies
358 relative to CCK+BC to PV+BC connections. While we were able to capture much with our many 2D
359 visualization plots from our thousands of simulations, further insights may be possible by doing
360 theoretical analyses of the PRM. This type of extensive exploration can be done using such reduced
361 models that have much less parameters relative to detailed models. Importantly, as the PRM was
362 built based on precise hypotheses developed from the biophysically detailed FSM, the predictions
363 arising have more biological plausibility regarding cell type specifics, relative to a 'generic' PRM. As
364 tools to identify and target CCK+BCs have been developed (*Dudok et al., 2021a*), we can envisage
365 designing experiments to directly test predictions arising from our work.

366 The initiation of theta rhythms by the PYR cell population in the hippocampus is also likely to be
367 the case in the biological system since the existence of 'threshold behaviour' in initiating hippocam-
368 pus population bursts has been shown before by *de la Prida et al.* (*2006*). Also, theta-resonant be-
369 haviour is expressed by PYR cells (*Hu et al., 2002*, *2009*). Interestingly, in another network modelling
370 study, the necessity of PYR cells to be near their threshold for firing was exploited to explain how
371 reduced excitatory fluctuations could lead to hyper-excitability in mouse models of Rett syndrome
372 (*Ho et al., 2014*).

373 The high frequency gamma rhythms seen in the model LFP (entwined with the slower frequency
374 theta rhythm) is more akin to the so-called ING (interneuron network gamma) rather than PING
375 (pyramidal-interneuron network gamma) mechanism (*Whittington et al., 2000*). That is, the PV+
376 and CCK+ BC networks have appropriate 'input and balance' to create coherent network output at
377 gamma frequencies, which is then imposed onto the PYR cell population. It is not a PING mech-
378 anism since gamma coherence does not (overall) rely on phasic input from PYR cells. The fact
379 that there is a phasic aspect to the theta/gamma rhythms in the model is related to the described
380 PYR cell clustering aspects. PING and ING certainly help us think about what sort of excitatory
381 and inhibitory balances might be key, but the additional cell types and the multi-modal oscillation
382 considerations here supercede these classical ideas. Naturally, what ultimately matters is what

experiments can be done to differentiate and understand the contributions from the various excitatory and inhibitory cell types in producing the circuit output, such as considered for visual cortex (*Tiesinga and Sejnowski, 2009*).

Our results are of course limited by what exists in the detailed FSM which was put together as carefully as possible given a 'knowledge base' of the available experimental data at the time (*Bezaire and Soltesz, 2013*). For example, we did not try to include PYR cell to CCK+BC connections in the PRM since they are not present in the FSM even though such connections possibly exist (*Dudok et al., 2021a*). Also, we did not include CCK+BC to PYR cell connections in the PRM even though they are present in the FSM. This does not negate the PRM results here. Rather, our interpretation would be that CCK+BC to PV+BC connections are more critical rhythm controllers than connections from CCK+BCs to PYR cells. We note that the AACs form strong connections with the PYR cells in the FSM and it is likely that they contribute to the termination of the theta burst along with the PV+BCs and BiCs by providing adequate inhibition and contributing to the excitatory-inhibitory balance necessary for theta rhythms (*Chatzikalymniou et al., 2021*).

While the theta mechanism presented in this study is based on the specific connectivity of the FSM network, the relative strength of connections between inhibitory populations evidently changes across the septo-temporal axis of the CA1 and across layers (*Soltesz and Losonczy, 2018*; *Navas-Olive et al., 2020*). *Navas-Olive et al.* (*2020*) have shown that PV+BCs preferentially innervate PYR cells at the deep sublayers while CCK+BCs are more likely to target the superficial PYR cells. Also, there is different innervation of PYR cells by BiCs and OLM cells in deep versus superficial PYR cells. How these differential connectivities affect theta-gamma rhythm control could be understood by examining various dynamic balances in the PRM. Further, specific known motifs that include VIP+ cell types (*Guet-McCreight et al., 2020*) are indirectly encompassed in the PRM via the inputs received by the different cell types and so their contributions can be indirectly considered in the theta/gamma mechanisms. Moving forward, one could imagine expanding the PRM to include additional cell type populations and connectivities to develop further hypotheses and to obtain predictions for experimental examination.

The plethora of inhibitory cell types with particular biophysical characteristics and connectivities in the hippocampus (*Pelkey et al., 2017*) make it challenging to figure out their particular contributions to dynamic network oscillations in the behaving animal. As theta and gamma oscillations and their coupling reflect cognitive processing and are potential disease biomarkers, *and* involve the various inhibitory cell types, we cannot ignore the potential roles played by these different types of interneurons. Interestingly, it has been shown that timescale gradients are significantly correlated with inhibitory cell-type markers (*Gao et al., 2020*). In conclusion, our work presented here shows that we can determine specific contributing roles of various inhibitory cell types by developing hypothesis-driven population rate models from detailed biophysical models. As tools to identity and control particular inhibitory cell types become more available, one can imagine leveraging these tractable PRM models for prediction and experimental design.

Methods

Detailed CA1 microcircuit: full-scale model (FSM)

The original fullscale CA1 microcircuit repository which can be found at ModelDB at: https://senselab.med.yale.edu/ModelDB/showModel.cshtml?model=187604. A new model version in python is now also available at: https://github.com/dhadjia1/ca1-microcircuit. Analysis of simulation outputs can be recreated using the publicly available SimTracker tool (*Bezaire et al., 2016a*). Documentation on SimTracker and installation instructions can be found at: https://simtrackercode.readthedocs.io/en/compiled/. It is recommended that users install SimTracker first and then install and register the CA1 model under SimTracker, to take advantage of the visualization functionalities of the SimTracker package. This tool is offered both as a stand-alone, compiled version for those without access to MATLAB (for Windows, Mac OS X, and Linux operating systems), and as a collection of MATLAB scripts for those with MATLAB access. Once the SimTracker and the CA1 repository are installed, users can run simulations either on their local machines using a small scale of the CA1 network, or on supercomputers as needed for full scale network simulations. To reproduce the findings presented here, one needs to first familiarize oneself with the CA1 microcircuit background and code.

A 10% 'slice' of the FSM (*Bezaire et al., 2016b*) is used in *Chatzikalymniou et al.* (*2021*). It is created from the FSM by reducing the volume and the number of cells by a tenth, as well as dividing all the connections in the network by a factor of ten so that we have a 'slice' and not a normalization of the FSM. The grid search is carried out using this model. In the FSM there are eight different inhibitory cell types and excitatory PYR cells. All of these cell types are connected in empirically specific ways based on an extensive knowledge-based review of the literature (*Bezaire and Soltesz, 2013*). The cells are evenly distributed within the various layers of the CA1 (stratum lacunosum-moleculare, radiatum, pyramidale, oriens) in a three-dimensional prism. Afferent inputs from CA3 and entorhinal cortex (EC) are also included in the form of Poisson-distributed spiking units from artificial CA3 and EC cells (referred to as 'other input' in TABLE 1). We note that although there are layer-dependent specifics regarding how the different cell types are arranged in the FSM, there are not any differences along the longitudinal axis. As such, the connection probabilities in any particular part of the longitudinal axis would be the same. Power spectral densities of FSM LFP output shown in FIGURES 1-2 are generated using a Welch periodogram python code -the same as that used in analyzing the population rate model described below.

Input currents to individual cells of the FSM

In order to obtain the input currents received by a cell in the FSM, the Network Clamp tool of the SimTracker software package (*Bezaire et al., 2016a*) was used. Using data obtained from the full-scale CA1 microcircuit simulations of *Bezaire et al.* (*2016b*) that are available on the CRCNS repository at: https://portal.nersc.gov/project/crcns/download/index.php, and the Network Clamp tool, one can explore the activity of any single neuron within the network. In this manner, we investigated five PYR cells and the input currents each of them received from all the other cell types in the network in the control network. We computed the mean net input current (-9.35 nA) across these five PYR cells, as well as the standard deviation in the net input current (0.13 nA). From a periodogram of the FSM of Bezaire et al, the theta frequency is 8.5 Hz. From the linear correlation between theta frequency and input current that we previously obtained (*Chatzikalymniou et al., 2021*), this frequency value would be due to an input current around 10 nA. Thus, the computed net input current here reasonably agrees with this relationship.

Grid search details using the network clamp technique

Using the Network Clamp tool, we can take a snapshot of the incoming synaptic input received by any particular cell in the network. We used it to undertake an in-depth exploration of the control of PV+BC activity due to inputs from other cell types. We applied it as follows: First, we obtained the output of an initial full-network simulation and ran network clamp simulations on a PV+BC. We altered the incoming afferent synapse weights (but not the incoming spike trains) and examined

471 how PV+BC activity was affected. This approach gives an estimate of how the synaptic weights
472 affect the PV+BC firing. From this, one can gain insight into how the post-synaptic weights might
473 affect the full network simulations.

474   The manner in which we undertook our exploration is illustrated in FIGURE 7. We used the
475 following pipeline of analysis:

476   1. Explore the post-synaptic weights onto a given PV+BC. Starting from a given set of reference
477   values (r.v.), vary the post-synaptic weights from all eight pre-synaptic cell types to the PV+BC,
478   and search the range of post-synaptic weights for each pre-synaptic cell type. The range used
479   is [-50% (r.v.), +50% (r.v.), 25%] (*start value*, *end value*, *step*), and as such it contains 5 values
480   which are: -50% (r.v.) | -25% (r.v.) | r.v. | +25% (r.v.) | +50% (r.v.). Explore the co-variation of
481   these values. Since every post-synaptic weight can take 5 values and that we explore a set of
482   eight post-synaptic weights, we have a total of 5^8 = 390,594 configurations.
483   2. Perform network clamp simulations for all configurations and store the voltage trace of the
484   PV+BC for each configuration.
485   3. Calculate the inter-spike intervals (ISIs) of every voltage trace using the open-source eFEL
486   library (https://github.com/BlueBrain/eFEL).
487   4. Plot the mean ISI across all configurations. This is shown in FIGURE 7.

Observations

489 In FIGURE 7, we show the result of a grid search representing the co-variation of eight post-synaptic
490 conductances. Following the simple visualization scheme shown in FIGURE 7A, we can easily dis-
491 cern the effect that each presynaptic cell has on the firing rate of the PV+BC. We distinguish a
492 number of patterns. As expected, incrementally strengthening the inhibitory PV+BCs post-synaptic
493 weights decreases the PV+BC firing rate (larger ISIs). However, for a critical value of the CCK+BC
494 to PV+BC conductance, we noticed a sudden decrease in the PV+BCs firing frequency which can
495 be up to 20Hz. This transition always occurred at a critical value of the CCK+BC to the PV+BC con-
496 ductance. Once that critical value is reached, a small increase in the rest of the conductances,
497 especially the PV+BC to PV+BC, mediates an abrupt elevation of the PV+BC mean firing rate (by
498 means of ISI). This observation reveals that, provided that the network operates close to this criti-
499 cal point, small changes in the CCK+BC activity can induce a sudden change (increase or decrease)
500 of the PV+BC firing rate. Such a critical value always exists regardless of the combination of the
501 rest of the post-synaptic conductances.

502   In essence, our grid search shows that if one sits close to a critical point (a point representing
503 a post-synaptic conductance configuration in close to a sharp transition of the PV+BC ISI), a small
504 decrease in the CCK+BC to PV+BC conductance induces a vast increase in the firing rate of the
505 PV+BCs, even by 20 Hz. This would support the argument that a strong disinhibition of the PV+BCs,
506 mediated by the CCK+BCs can induce a sudden increase in the PV+BC firing rate and mediate the
507 sharp termination of the PYR population. If the FSM dynamics follow those of our grid search of
508 the clamped network model, then a strong inhibition of the CCK+BCs would effectively release the
509 PV+BCs from the CCK+BC inhibition causing a sudden increase in the firing rate of the PV+BC.

High performance computing simulations

511 We implement our simulations on Scinet (*Loken et al., 2010*; *Ponce et al., 2019*) on the Niagara
512 clusters, using 10-12 nodes per simulation with 40 cores per node. Each FSM simulation takes
513 approximately 8 hours real time to be executed. Several FSM simulations were carried out with
514 removal of particular connection. The grid search of post-synaptic weights was also carried out on
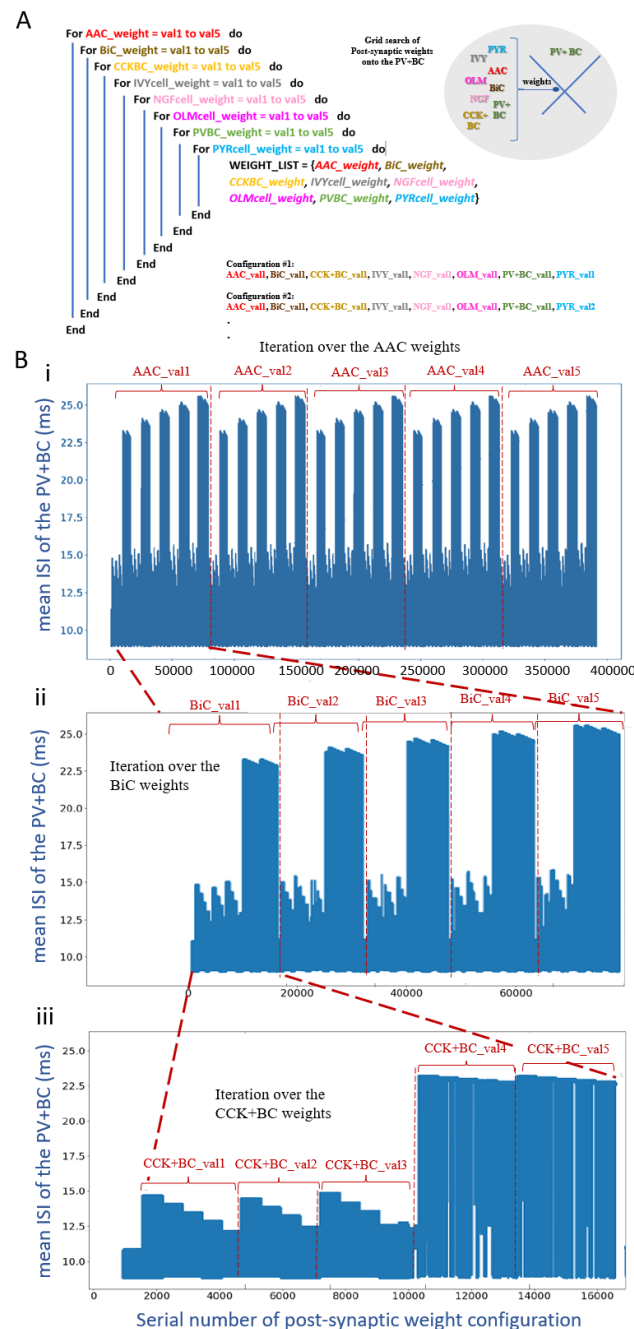515 scinet using 1 node (40 cores per node) and took approximately 3 hours.

Figure 7. The PV+BC ISIs as a function of the configuration number of the post-synaptic weight combinations.

We iterate over the post-synaptic PV+BC weights according to the process described Methods. **A.** Recursive algorithm of the grid search over a range of five post-synaptic weights per cell type. **B.** Iteration over the postsynaptic weights gives rise to a fractal-like pattern in which similar patterns recur at progressively smaller scales. (i) On the largest scale we identify a group of five repetitive motifs where each motif corresponds to a given AAC post-synaptic weight value. (ii) Within each of these motifs another group of five repetitive motifs corresponds to the five BiC post-synaptic weight values. (iii) Equally within each one of these five motifs another group of five similar motifs corresponds to the five CCK+BC post-synaptic weight values and so on. Incremental increases of the other five post-synaptic cell weights which don't influence PV+BC firing significantly.

516 FSM parameter value sets

517 To rationalize the focus on a subset of the several different cell types in the FSM, we considered
518 the 'Other Input' (external drives) received by different cell types (see TABLE 1). From this table, it
519 is clear that AACs receive the smallest amount of other input.

Cell Type	Other Input	Number of Cells
PYR cell	2,914	311,500
CCK-BC	3,327	3,600
PV-BC	2,661	5,530
BiC	1,864	2,210
OLM cell	0 (NONE)	1,640
AAC	1,117	1,470
Ivy cell	1,154	8,810
SCA cell	1,680	400
NGF cell	3,661	3,580

Table 1. Number of cells and other input to each cell type in the FSM of *Bezaire et al.* (*2016b*).

520 As well, we extracted connectivities between all the different cell types in the FSM. Specifically,
521 we compute an effective weight (EW) which is the connection probability times the synaptic weight.
522 The EWs are shown in TABLES 2 and 3. Note that computed EW values are multiplied by 100 to
523 reduce decimal zeroes.

Connection Coupling	Number of Connections	Connection Probability	Synaptic Weight (nS)	EW Value (× 100)
PYR->PYR	197	0.00063	70.0	4.4
PYR->BiC	3	0.0014	5.7	0.80
PYR->PV	8	0.0015	2.1	0.32
PYR->OLM	13	0.0079	0.6	0.47
PYR->CCK	-	-	-	0 (NONE)
PYR->AAC	1	0.00068	0.12	0.0082
PYR->Ivy	-	-	-	0 (NONE)
PYR->NGF	-	-	-	0 (NONE)
PYR->SCA	-	-	-	0 (NONE)
BiC->BiC	16	0.0072	5.1	3.7
BiC->PYR	1410	0.0045	5.1	2.3
BiC->CCK	26	0.0072	8.0	5.8
BiC->PV	40	0.0072	90.0	64.8
BiC->OLM	29	0.018	0.2	0.35
BiC->AAC	11	0.0075	6.0	4.5
BiC->Ivy	12	0.0014	5.0	0.68
BiC->NGF	-	-	-	0 (NONE)
BiC->SCA	3	0.0075	8.0	6.0
CCK->CCK	35	0.0097	3.6	3.5
CCK->PV	18	0.0033	72.0	23.8
CCK->PYR	1125	0.0036	4.2	1.5
CCK->BiC	7	0.0032	5.6	1.8
CCK->OLM	9	0.0055	5.6	3.1
CCK->AAC	5	.0034	5.6	1.9
CCK->Ivy	20	0.0023	2.4	0.55
CCK->NGF	-	-	-	0 (NONE)
CCK->SCA	3	0.0075	5.6	4.2
PV->PV	39	0.0071	1.6	1.1
PV->PYR	958	0.0031	2.2	0.7
PV->CCK	25	0.0069	1.2	0.8
PV->BiC	16	0.0072	2.9	2.1
PV->OLM	-	-	-	0 (NONE)
PV->AAC	10	0.0068	0.12	0.8
PV->Ivy	13	0.0015	0.16	0.024
PV->NGF	-	-	-	0 (NONE)
PV->SCA	2	0.005	0.6	0.3
OLM->OLM	6	0.0037	1.2	4.4
OLM->PV	27	0.0049	11.0	5.4
OLM->CCK	88	0.024	12.0	28.8
OLM->BiC	11	0.0050	1.1	0.55
OLM->PYR	1520	0.0049	3.0	1.5
OLM->AAC	7	0.0048	1.2	0.57
OLM->Ivy	-	-	-	0 (NONE)
OLM->NGF	28	0.0078	0.98	0.77
OLM->SCA	10	0.025	1.5	3.8

Table 2. Connectivities based on *Bezaire et al.* (*2016b*) Appendix values for PYR cells, BiCs, CCK-BCs, PV-BCs and OLM cells.

Connection Coupling	Number of Connections	Connection Probability	Synaptic Weight (nS)	EW Value (× 100)
AAC->AAC	-	-	-	0 (NONE)
AAC->PYR	1271	0.0041	6.9	2.82
AAC->BiC,PV,OLM,CCK,Ivy,NGF,SCA	-	-	-	0 (NONE)
Ivy->Ivy	24	0.0027	0.57	0.16
Ivy->PYR	1485	0.0048	0.41	0.20
Ivy->BiC	6	0.0027	0.77	0.21
Ivy->PV	15	0.0027	7.0	1.90
Ivy->OLM	25	0.015	0.57	0.87
Ivy->CCK	39	0.011	0.37	0.40
Ivy->NGF	11	0.0031	0.57	0.18
Ivy->SCA	5	0.013	0.37	0.46
Ivy->AAC	4	0.0027	0.57	0.16
NGF->NGF	17	0.0047	1.6	0.76
NGF->PYR	1218	0.0039	0.65	0.25
NGF->BiC,PV,OLM,CCK,Ivy,SCA,AAC	-	-	-	0 (NONE)
SCA->SCA	6	0.015	6.0	9.0
SCA->PYR	1558	0.005	4.6	2.3
SCA->BiC	7	0.0032	3.6	1.15
SCA->PV	14	0.0025	7.8	1.95
SCA->OLM	8	0.0049	5.1	2.5
SCA->CCK	50	0.014	5.1	7.1
SCA->Ivy	44	0.0050	5.1	2.6
SCA->NGF	-	-	-	0 (NONE)
SCA->AAC	4	0.0027	3.6	0.98

Table 3. Connectivities based on *Bezaire et al.* (*2016b*) Appendix values for AACs, Ivy cells, NGF cells and SCA cells.

524 Population Rate Model (PRM)

525 In order to disambiguate the respective role of cell types and their mutual connectivity motifs in
526 the generation and control of theta-gamma coupling in the hippocampus, we developed a reduced,
527 system-level population rate model (PRM). This phenomenological model combines connections
528 and cell types that are identified as critical in generating oscillatory activity and theta-gamma cou-
529 pling based on previous work (*Chatzikalymniou et al., 2021*) and systematic parameter exploration
530 of the detailed model (*Bezaire et al., 2016b*) here. The purpose of the PRM is the identification and
531 analysis of key mechanisms involved in cross-frequency interactions and oscillatory control over
532 hippocampal microcircuits, following the formalism of population-scale mean-field models.

533 The PRM describes the time evolution of PYR cell, CCK+BC, PV+BC and BiC mean firing rates
534 ($r_{PYR}, r_{BiC}, r_{CCK}$ and r_{PV}) as a function of their mutual connectivity motif (FIGURE 3), synaptic weights
535 ($w_{n \to m}$, for $n, m = PYR, BiC, CCK$ and/or PV) membrane rate constants ($\alpha_{PYR}, \alpha_{BiC}, \alpha_{CCK}$ and α_{PV}),
536 synaptic and axonal delays (τ), population-specific inputs ($i_{PYR}, i_{BiC}, i_{CCK}$ and i_{PV}) as well as intrinsic
537 random fluctuations, and how these collectively contribute to the generation of rhythmic firing rate
538 modulations. The resulting model builds on the well-known *Wilson and Cowan* (*1972*) formalism,
539 resulting in the following set of nonlinear delayed stochastic differential equations,

$$\alpha_{PYR}^{-1} \frac{dr_{PYR}}{dt} = -r_{PYR} + r_o f[I_{PYR}] + \sqrt{2D_{PYR}}\xi_{PYR}(t) \tag{1}$$

$$\alpha_{BiC}^{-1} \frac{dr_{BiC}}{dt} = -r_{BiC} + r_o f[I_{BiC}] + \sqrt{2D_{BiC}}\xi_{BiC}(t) \tag{2}$$

$$\alpha_{CCK}^{-1} \frac{dr_{CCK}}{dt} = -r_{CCK} + r_o f[I_{CCK}] + \sqrt{2D_{CCV}}\xi_{CCK}(t) \tag{3}$$

$$\alpha_{PV}^{-1} \frac{dr_{PV}}{dt} = -r_{PV} + r_o f[I_{PV}] + \sqrt{2D_{PV}}\xi_{PV}(t) \tag{4}$$

540 where r_o represents the maximal firing rate of the neurons. Fluctuations in mean firing rates
541 results from the nonlinear integration of presynaptic inputs I_m (here and below, $m = PYR, BiC, CCK$
542 or PV) combined to the effect of random perturbations of variance D_m in which ξ_m are uncorrelated
543 zero mean Gaussian white noise process such that $< \xi_m(t)\xi_n(s) >= \delta_{nm}(t-s)$, where $<>$ is a temporal
544 average and δ is the Dirac delta function. Presynaptic inputs I_m scale firing rates through the firing
545 rate response function

$$f[I_m] = \frac{1}{1 + e^{-\beta I_m}} \tag{5}$$

546 whose gain β reflects the steepness of the response. The presynaptic inputs $I_{PYR}, I_{BiC}, I_{CCK}$ and
547 I_{PV} are given by

$$I_{PYR} = w_{PYR \to PYR} r_{PYR}(t-\tau) + w_{BiC \to PYR} r_{BiC}(t-\tau) + w_{PV \to PYR} r_{PV}(t-\tau) + i_{PYR} \tag{6}$$

$$I_{BiC} = w_{PYR \to BiC} r_{PYR}(t-\tau) + i_{BiC} \tag{7}$$

$$I_{CCK} = w_{CCK \to CCK} r_{CCK}(t-\tau) + w_{PV \to CCK} r_{PV}(t-\tau) + i_{CCK} \tag{8}$$

$$I_{PV} = w_{CCK \to PV} r_{CCK}(t-\tau) + w_{PV \to PV} r_{PV}(t-\tau) + w_{PYR \to PV} r_{PYR}(t-\tau) + i_{PV} \tag{9}$$

548 Cell-type specific inputs ($i_{PYR}, i_{BiC}, i_{CCK}$ and i_{PV}) represent external stimuli modulating the excitabil-
549 ity of the different cell populations. A minimal time delay of $\tau = 5ms$ was included to represent
550 finite axonal and synaptic conduction. The parameters α_m represents the membrane rate constant
551 and sets the time scale at which populations respond to stimuli. The coupling constants $w_{m \to n}$ rep-
552 resent the synaptic weights from population m to population n for $n, m = PYR, BiC, CCK$ and/or
553 PV. Reference parameter values that produce the control output shown in FIGURE 4A are given in
554 TABLE 4.

555 The PRM exhibits co-modulated oscillations within the gamma and theta frequency ranges.
556 Since the PYR cells constitute the majority of the cells in the network, it is reasonable to consider
557 the PYR cell activity as an LFP proxy. In the absence of multi-compartment representations, vari-
558 ous LFP proxies have been used (*Einevoll et al., 2013*) that include number of 'firing cells' (*Traub*

Symbol	Definition	Value
β	Response function gain	10au
τ	Conduction delay	5ms
α_{PYR}	PYR cell rate constant	50Hz
α_{BiC}	BiC rate constant	50Hz
α_{CCK}	CCK+BC rate constant	80Hz
α_{PV}	PV+BC rate constant	100Hz
$w_{PYR \to PYR}$	$PYR \to PYR$ coupling	0.03au
$w_{PYR \to BiC}$	$PYR \to BiC$ coupling	0.04au
$w_{PYR \to PV}$	$PYR \to PV$ coupling	0.02au
$w_{BiC \to PYR}$	$BiC \to PYR$ coupling	-0.03au
$w_{CCK \to CCK}$	$CCK \to CCK$ coupling	-0.15au
$w_{CCK \to PV}$	$CCK \to PV$ coupling	-0.15au
$w_{PV \to PV}$	$PV \to PV$ coupling	-0.055au
$w_{PV \to PYR}$	$PV \to PYR$ coupling	-0.04au
$w_{PV \to CCK}$	$PV \to CCK$ coupling	-0.075au
i_{PYR}	Input to PYR cells	0.07au
i_{BiC}	Input to BiCs	-1.05au
i_{CCK}	Input to CCK+BCs	0.7au
i_{PV}	Input to PV+BCs	0.45au
D_{PYR}	Noise variance to PYR cells	0.001au
D_{BiC}	Noise variance to BiCs	0.001au
D_{CCK}	Noise variance to CCK+BCs	0.001au
D_{PV}	Noise variance to PV+BCs	0.001au
r_o	Maximum firing rate	30Hz

Table 4. Reference parameter values for the PRM.

---

559 *et al., 1992*) which is in essence the PYR cell activity in the PRM. Co-modulated oscillations result
560 from a combination of excitation-inhibition relaxation oscillations and delay-induced oscillations
561 whose peak frequency and power - and resulting dominance - are controlled by a combination of
562 parameters which we explore systematically in FIGURES 5 and 6.

Simulations and visualizations of the PRM

564 Each of the thousands of simulations was performed for a duration of 2.0 s with a step size of
565 $dt = 0.001$ s. The differential equations were integrated using a forward Euler method and the
566 output from each of the four different cell type populations in the model was filtered using a band
567 pass filter. For consideration of the theta (θ) band frequency, the output was filtered between
568 $3 - 15$ Hz while for consideration of the gamma (γ) band frequency, the output was filtered be-
569 tween $15 - 100$ Hz. The peak frequency was obtained by finding the frequency corresponding to
570 the highest peak in a Welch periodogram (using the *welch* function of the *scipy.signal* module in
571 Python with $nperseg = 1024$). The power of the peak frequency was also recorded from the Welch
572 periodogram. Python code to automate the sets of simulations and create all the subsequent vi-
573 sualisations are given in: https://github.com/FKSkinnerLab/PRM.git

574 **Heat Maps and Contours:** Two-dimensional heat maps of θ and γ frequencies and power were
575 created for different sets of parameters. For each pair of parameter values that were explored,
576 the range of values for each parameter was divided into 300 equally spaced intervals, creating a
577 300x300 grid in the two dimensional parameter space. For each point in the grid, the model was
578 simulated using the corresponding values for the parameters being explored while keeping all the
579 other parameters at their reference values. The corresponding frequency and power for the θ and

580   γ bands were recorded for each point in the grid. Power contours were added to the frequency
581   heat maps to create the plots shown in FIGURES 5 and 6. Six evenly spaced contours were drawn
582   that are representative of the entire range of power values over that grid (using the *MaxNLocator*
583   function of the *matplotlib.ticker* module in Python), and were added to the frequency heat map.

584   **Power Difference Maps**: For comparing the relative power of the θ and γ oscillations, each of the
585   individual power maps were normalised within their range of values, and the difference of $(\theta - \gamma)$
586   normalized powers is calculated. A positive (negative) result indicates a stronger θ (γ) rhythm due
587   to its larger normalized power.

588   **Theta Frequency Plots**: For each of the θ frequency plots shown in FIGURES 5 and 6, one of the pa-
589   rameters was held constant at a value such that a range of θ frequencies over an entire range of val-
590   ues of the other parameter that was being explored had reasonably large power values. The other
591   parameter was varied across the chosen range and the θ frequency of the PYR cell was recorded
592   for each point after filtering the output. The ranges and constant values were chosen such that
593   the power of the θ oscillations never fell below 10% of its maximum value over the previously ex-
594   plored parameter space for the $i_{PYR} - w_{PYR \to PYR}$ and $w_{PV \to CCK} - w_{CCK \to PV}$ ranges, and 25% for the
595    $w_{BiC \to PYR} - w_{PYR \to BiC}$ and $w_{PV \to PYR} - w_{PYR \to PV}$ ranges.

References

Axmacher N, Henseler MM, Jensen O, Weinreich I, Elger CE, Fell J. Cross-frequency coupling supports multi-item working memory in the human hippocampus. Proceedings of the National Academy of Sciences. 2010 Feb; 107(7):3228–3233. https://www.pnas.org/doi/10.1073/pnas.0911531107, doi: 10.1073/pnas.0911531107, publisher: Proceedings of the National Academy of Sciences.

Bandarabadi M, Boyce R, Gutierrez Herrera C, Bassetti CL, Williams S, Schindler K, Adamantidis A. Dynamic modulation of theta-gamma coupling during rapid eye movement sleep. Sleep. 2019 Dec; 42(12). doi: 10.1093/sleep/zsz182.

Bezaire MJ, Raikov I, Burk k, Armstrong C, Soltesz I. SimTracker tool and code template to design, manage and analyze neural network model simulations in parallel NEURON. bioRxiv. 2016; https://www.biorxiv.org/content/early/2016/10/19/081927, doi: 10.1101/081927.

Bezaire MJ, Raikov I, Burk K, Vyas D, Soltesz I. Interneuronal mechanisms of hippocampal theta oscillation in a full-scale model of the rodent CA1 circuit. eLife. 2016 Dec; 5:e18566. https://elifesciences.org/content/5/e18566v1, doi: 10.7554/eLife.18566.

Bezaire MJ, Soltesz I. Quantitative assessment of CA1 local circuits: Knowledge base for interneuron-pyramidal cell connectivity. Hippocampus. 2013 May; doi: 10.1002/hipo.22141.

Buzsaki G. Hippocampus. Scholarpedia. 2011; 6(1):1468. http://www.scholarpedia.org/article/Hippocampus, doi: 10.4249/scholarpedia.1468.

Buzsáki G. Rhythms of the Brain. 1 ed. Oxford University Press, USA; 2006.

Buzsáki G. Theta oscillations in the hippocampus. Neuron. 2002 Jan; 33(3):325–340. http://www.ncbi.nlm.nih.gov/pubmed/11832222.

Buzsáki G, Lai-Wo S L, Vanderwolf CH. Cellular bases of hippocampal EEG in the behaving rat. Brain Research Reviews. 1983 Oct; 6(2):139–171. https://www.sciencedirect.com/science/article/pii/0165017383900371, doi: 10.1016/0165-0173(83)90037-1.

Buzsáki G, Moser EI. Memory, navigation and theta rhythm in the hippocampal-entorhinal system. Nature neuroscience. 2013 Jan; 16:130–138. doi: 10.1038/nn.3304.

Canolty RT, Knight RT. The functional role of cross-frequency coupling. Trends in Cognitive Sciences. 2010 Nov; 14(11):506–515. http://www.sciencedirect.com/science/article/pii/S1364661310002068, doi: 10.1016/j.tics.2010.09.001.

Chatzikalymniou AP, Gumus M, Skinner FK. Linking minimal and detailed models of CA1 microcircuits reveals how theta rhythms emerge and their frequencies controlled. Hippocampus. 2021; 31(9):982–1002. http://onlinelibrary.wiley.com/doi/abs/10.1002/hipo.23364, doi: 10.1002/hipo.23364, _eprint: https://onlinelibrary.wiley.com/doi/pdf/10.1002/hipo.23364.

Colgin LL. Theta–gamma coupling in the entorhinal–hippocampal system. Current Opinion in Neurobiology. 2015 Apr; 31:45–50. http://www.sciencedirect.com/science/article/pii/S0959438814001639, doi: 10.1016/j.conb.2014.08.001.

Colgin LL. Rhythms of the hippocampal network. Nature Reviews Neuroscience. 2016 Apr; 17(4):239–249. doi: 10.1038/nrn.2016.21.

Colgin LL, Denninger T, Fyhn M, Hafting T, Bonnevie T, Jensen O, Moser MB, Moser EI. Frequency of gamma oscillations routes flow of information in the hippocampus. Nature. 2009; 462(7271):353–357. doi: 10.1038/nature08573.

Dudok B, Klein PM, Hwaun E, Lee BR, Yao Z, Fong O, Bowler JC, Terada S, Sparks FT, Szabo GG, Farrell JS, Berg J, Daigle TL, Tasic B, Dimidschstein J, Fishell G, Losonczy A, Zeng H, Soltesz I. Alternating sources of perisomatic inhibition during behavior. Neuron. 2021 Mar; 109(6):997–1012.e9. https://www.sciencedirect.com/science/article/pii/S0896627321000039, doi: 10.1016/j.neuron.2021.01.003.

Dudok B, Szoboszlay M, Paul A, Klein PM, Liao Z, Hwaun E, Szabo GG, Geiller T, Vancura B, Wang BS, McKenzie S, Homidan J, Klaver LMF, English DF, Huang ZJ, Buzsáki G, Losonczy A, Soltesz I. Recruitment and inhibitory action of hippocampal axo-axonic cells during behavior. Neuron. 2021 Dec; 109(23):3838–3850.e8. https://www.cell.com/neuron/abstract/S0896-6273(21)00706-6, doi: 10.1016/j.neuron.2021.09.033, publisher: Elsevier.

646 **Ecker A**, Romani A, Sáray S, Káli S, Migliore M, Falck J, Lange S, Mercer A, Thomson AM,
647 Muller E, Reimann MW, Ramaswamy S. Data-driven integration of hippocampal CA1 synap-
648 tic physiology in silico. Hippocampus. 2020; n/a(n/a). doi: 10.1002/hipo.23220, _eprint:
649 https://onlinelibrary.wiley.com/doi/pdf/10.1002/hipo.23220.

650 **Einevoll GT**, Kayser C, Logothetis NK, Panzeri S. Modelling and analysis of local field potentials for studying the
651 function of cortical circuits. Nature Reviews Neuroscience. 2013 Nov; 14(11):770–785. doi: 10.1038/nrn3599.

652 **Eriksson O**, Bhalla US, Blackwell KT, Crook SM, Keller D, Kramer A, Linne ML, Saudargienė A, Wade RC, Hell-
653 gren Kotaleski J. Combining hypothesis- and data-driven neuroscience modeling in FAIR workflows. eLife.
654 2022 Jul; 11:e69013. https://doi.org/10.7554/eLife.69013, doi: 10.7554/eLife.69013, publisher: eLife Sciences
655 Publications, Ltd.

656 **Fasano C**, Rocchetti J, Pietrajtis K, Zander JF, Manseau F, Sakae DY, Marcus-Sells M, Ramet L, Morel LJ, Carrel
657 D, Dumas S, Bolte S, Bernard V, Vigneault E, Goutagny R, Ahnert-Hilger G, Giros B, Daumas S, Williams S,
658 El Mestikawy S. Regulation of the Hippocampal Network by VGLUT3-Positive CCK- GABAergic Basket Cells.
659 Frontiers in Cellular Neuroscience. 2017; 11. doi: 10.3389/fncel.2017.00140.

660 **Ferguson KA**, Chatzikalymniou AP, Skinner FK. Combining Theory, Model, and Experiment to Explain How
661 Intrinsic Theta Rhythms Are Generated in an In Vitro Whole Hippocampus Preparation without Oscillatory
662 Inputs. eNeuro. 2017 Aug; 4(4). doi: 10.1523/ENEURO.0131-17.2017.

663 **Ferguson KA**, Skinner FK. Hippocampal Theta, Gamma, and Theta/Gamma Network Models. In: Jaeger D, Jung
664 R, editors. *Encyclopedia of Computational Neuroscience* Springer; 2015.p. 1340–1352. https://doi.org/10.1007/
665 978-1-4614-6675-8_27, doi: 10.1007/978-1-4614-6675-8_27.

666 **Fishell G**, Kepecs A. Interneuron Types as Attractors and Controllers. Annual Review of Neuroscience. 2020 Jul;
667 43(1):1–30. http://www.annualreviews.org/doi/10.1146/annurev-neuro-070918-050421, doi: 10.1146/annurev-
668 neuro-070918-050421, publisher: Annual Reviews.

669 **Freund TF**, Buzsáki G. Interneurons of the hippocampus. Hippocampus. 1996; 6(4):347–470. doi:
670 10.1002/(SICI)1098-1063(1996)6:4<347::AID-HIPO1>3.0.CO;2-I.

671 **Freund TF**. Interneuron Diversity series: Rhythm and mood in perisomatic inhibition. Trends in Neuro-
672 sciences. 2003 Sep; 26(9):489–495. http://www.sciencedirect.com/science/article/pii/S0166223603002273, doi:
673 10.1016/S0166-2236(03)00227-3.

674 **Freund TF**, Katona I. Perisomatic Inhibition. Neuron. 2007 Oct; 56(1):33–42. http://www.sciencedirect.com/
675 science/article/pii/S0896627307007106, doi: 10.1016/j.neuron.2007.09.012.

676 **Gao R**, van den Brink RL, Pfeffer T, Voytek B. Neuronal timescales are functionally dynamic and shaped
677 by cortical microarchitecture. eLife. 2020 Nov; 9:e61277. https://doi.org/10.7554/eLife.61277, doi:
678 10.7554/eLife.61277, publisher: eLife Sciences Publications, Ltd.

679 **Goutagny R**, Gu N, Cavanagh C, Jackson J, Chabot JG, Quirion R, Krantic S, Williams S. Alterations in hip-
680 pocampal network oscillations and theta-gamma coupling arise before amyloid beta overproduction in a
681 mouse model of Alzheimer's disease. The European Journal of Neuroscience. 2013; 37(12):1896–1902. doi:
682 10.1111/ejn.12233.

683 **Goutagny R**, Jackson J, Williams S. Self-generated theta oscillations in the hippocampus. Nature Neuroscience.
684 2009 Dec; 12(12):1491–1493. http://www.ncbi.nlm.nih.gov/pubmed/19881503, doi: 10.1038/nn.2440.

685 **Guet-McCreight A**, Skinner FK, Topolnik L. Common Principles in Functional Organization of VIP/Calretinin
686 Cell-Driven Disinhibitory Circuits Across Cortical Areas. Frontiers in Neural Circuits. 2020; 14.
687 https://www.frontiersin.org/articles/10.3389/fncir.2020.00032/full?utm_source=F-AAE&utm_medium=
688 EMLF&utm_campaign=MRK_1356251_55_Neuros_20200618_arts_A, doi: 10.3389/fncir.2020.00032,
689 publisher: Frontiers.

690 **Hamm V**, Héraud C, Cassel JC, Mathis C, Goutagny R. Precocious Alterations of Brain Oscillatory Activity in
691 Alzheimer's Disease: A Window of Opportunity for Early Diagnosis and Treatment. Frontiers in Cellular
692 Neuroscience. 2015; p. 491. http://journal.frontiersin.org.myaccess.library.utoronto.ca/article/10.3389/fncel.
693 2015.00491/full?utm_source=newsletter&utm_medium=email&utm_campaign=Neuroscience-w6-2016, doi:
694 10.3389/fncel.2015.00491.

695 **Ho ECY**, Eubanks JH, Zhang L, Skinner FK. Network Models Predict that Reduced Excitatory Fluctuations Can
696 Give Rise to Hippocampal Network Hyper-Excitability in MeCP2-Null Mice. PLoS ONE. 2014 Mar; 9(3):e91148.
697 http://dx.doi.org/10.1371/journal.pone.0091148, doi: 10.1371/journal.pone.0091148.

698 **Hu H**, Vervaeke K, Graham LJ, Storm JF. Complementary Theta Resonance Filtering by Two Spatially
699 Segregated Mechanisms in CA1 Hippocampal Pyramidal Neurons. The Journal of Neuroscience. 2009
700 Nov; 29(46):14472–14483. http://www.jneurosci.org.myaccess.library.utoronto.ca/content/29/46/14472, doi:
701 10.1523/JNEUROSCI.0187-09.2009.

702 **Hu H**, Vervaeke K, Storm JF. Two forms of electrical resonance at theta frequencies, generated by M-current,
703 h-current and persistent Na+ current in rat hippocampal pyramidal cells. The Journal of Physiology. 2002
704 Dec; 545(3):783–805. http://jp.physoc.org.myaccess.library.utoronto.ca/content/545/3/783, doi: 10.1113/jphys-
705 iol.2002.029249.

706 **Jackson J**, Goutagny R, Williams S. Fast and slow γ rhythms are intrinsically and independently generated
707 in the subiculum. The Journal of Neuroscience: The Official Journal of the Society for Neuroscience. 2011;
708 31(34):12104–12117. doi: 10.1523/JNEUROSCI.1370-11.2011.

709 **Karlsson AE**, Lindenberger U, Sander MC. Out of Rhythm: Compromised Precision of Theta-Gamma Coupling
710 Impairs Associative Memory in Old Age. Journal of Neuroscience. 2022 Mar; 42(9):1752–1764. http://www.
711 jneurosci.org/content/42/9/1752, doi: 10.1523/JNEUROSCI.1678-21.2021.

712 **Kepecs A**, Fishell G. Interneuron cell types are fit to function. Nature. 2014 Jan; 505(7483):318–326. doi:
713 10.1038/nature12983.

714 **Kitchigina VF**. Alterations of Coherent Theta and Gamma Network Oscillations as an Early Biomarker of
715 Temporal Lobe Epilepsy and Alzheimer's Disease. Frontiers in Integrative Neuroscience. 2018; 12. doi:
716 10.3389/fnint.2018.00036.

717 **Klausberger T**, Somogyi P. Neuronal Diversity and Temporal Dynamics: The Unity of Hippocampal Circuit
718 Operations. Science. 2008 Jul; 321(5885):53 –57. http://www.sciencemag.org/content/321/5885/53.abstract,
719 doi: 10.1126/science.1149381.

720 **Kragel JE**, VanHaerents S, Templer JW, Schuele S, Rosenow JM, Nilakantan AS, Bridge DJ. Hippocampal theta
721 coordinates memory processing during visual exploration. eLife. 2020 Mar; 9:e52108. https://doi.org/10.
722 7554/eLife.52108, doi: 10.7554/eLife.52108, publisher: eLife Sciences Publications, Ltd.

723 **Leão RN**, Mikulovic S, Leão KE, Munguba H, Gezelius H, Enjin A, Patra K, Eriksson A, Loew LM, Tort ABL, Kullander
724 K. OLM interneurons differentially modulate CA3 and entorhinal inputs to hippocampal CA1 neurons. Nature
725 Neuroscience. 2012; 15(11):1524–1530. doi: 10.1038/nn.3235.

726 **Lega B**, Burke J, Jacobs J, Kahana MJ. Slow-Theta-to-Gamma Phase–Amplitude Coupling in Human Hippocampus
727 Supports the Formation of New Episodic Memories. Cerebral Cortex. 2016; 26(1):268–278. https://academic.
728 oup.com/cercor/article/26/1/268/2367079, doi: 10.1093/cercor/bhu232.

729 **Loken C**, Gruner D, Groer L, Peltier R, Bunn N, Craig M, Teresa Henriques, Dempsey J, Yu CH, Chen J, Dursi
730 LJ, Chong J, Scott Northrup, Pinto J, Knecht N, Zon RV. SciNet: Lessons Learned from Building a Power-
731 efficient Top-20 System and Data Centre. Journal of Physics: Conference Series. 2010; 256(1):012026. http:
732 //stacks.iop.org/1742-6596/256/i=1/a=012026, doi: 10.1088/1742-6596/256/1/012026.

733 **McBain CJ**, Fisahn A. Interneurons unbound. Nature Reviews Neuroscience. 2001; 2(1):11–23. doi:
734 10.1038/35049047.

735 **Musaeus CS**, Nielsen MS, Musaeus JS, Høgh P. Electroencephalographic Cross-Frequency Coupling as a Sign
736 of Disease Progression in Patients With Mild Cognitive Impairment: A Pilot Study. Frontiers in Neuroscience.
737 2020 Aug; 14:790. https://www.ncbi.nlm.nih.gov/pmc/articles/PMC7431634/, doi: 10.3389/fnins.2020.00790.

738 **Navas-Olive A**, Valero M, Jurado-Parras T, Salas-Quiroga Ad, Averkin RG, Gambino G, Cid E, Prida LMdl. Multi-
739 modal determinants of phase-locked dynamics across deep-superficial hippocampal sublayers during theta
740 oscillations. Nature Communications. 2020; 11(1):1–14. https://www.nature.com/articles/s41467-020-15840-6,
741 doi: 10.1038/s41467-020-15840-6, number: 1.

742 **Pelkey KA**, Chittajallu R, Craig MT, Tricoire L, Wester JC, McBain CJ. Hippocampal GABAergic Inhibitory Interneu-
743 rons. Physiological Reviews. 2017 Oct; 97(4):1619–1747. http://physrev.physiology.org.myaccess.library.utoronto.
744 ca/content/97/4/1619, doi: 10.1152/physrev.00007.2017.

745 **Ponce M**, van Zon R, Northrup S, Gruner D, Chen J, Ertinaz F, Fedoseev A, Groer L, Mao F, Mundim BC, Nolta M,
746 Pinto J, Saldarriaga M, Slavnic V, Spence E, Yu CH, Peltier WR. Deploying a Top-100 Supercomputer for Large
747 Parallel Workloads: the Niagara Supercomputer. In: *Proceedings of the Practice and Experience in Advanced
748 Research Computing on Rise of the Machines (learning)* PEARC '19, Association for Computing Machinery; 2019.
749 p. 1–8. https://doi.org/10.1145/3332186.3332195, doi: 10.1145/3332186.3332195.

750 **de la Prida LM**, Huberfeld G, Cohen I, Miles R. Threshold behavior in the initiation of hippocampal pop-
751 ulation bursts. Neuron. 2006 Jan; 49(1):131–142. http://www.ncbi.nlm.nih.gov/pubmed/16387645, doi:
752 10.1016/j.neuron.2005.10.034.

753 **Radiske A**, Gonzalez MC, Conde-Ocazionez S, Rossato JI, Köhler CA, Cammarota M. Cross-Frequency
754 Phase-Amplitude Coupling between Hippocampal Theta and Gamma Oscillations during Recall Destabilizes
755 Memory and Renders It Susceptible to Reconsolidation Disruption. Journal of Neuroscience. 2020 Aug;
756 40(33):6398–6408. https://www.jneurosci.org/content/40/33/6398, doi: 10.1523/JNEUROSCI.0259-20.2020,
757 publisher: Society for Neuroscience Section: Research Articles.

758 **Robbe D**, Buzsáki G. Alteration of Theta Timescale Dynamics of Hippocampal Place Cells by a Cannabinoid
759 Is Associated with Memory Impairment. Journal of Neuroscience. 2009; 29(40):12597–12605. https://www.
760 jneurosci.org/content/29/40/12597, doi: 10.1523/JNEUROSCI.2407-09.2009.

761 **Skinner FK**, Rich S, Lunyov AR, Lefebvre J, Chatzikalymniou AP. A Hypothesis for Theta Rhythm Frequency
762 Control in CA1 Microcircuits. Frontiers in Neural Circuits. 2021; 15. https://www.frontiersin.org/articles/10.
763 3389/fncir.2021.643360/full?utm_source=F-AAE&utm_medium=EMLF&utm_campaign=MRK_1616048_
764 55_Neuros_20210504_arts_A, doi: 10.3389/fncir.2021.643360, publisher: Frontiers.

765 **Soltesz I**, Losonczy A. CA1 pyramidal cell diversity enabling parallel information processing in the hippocampus.
766 Nature Neuroscience. 2018 Apr; 21(4):484–493. https://www-nature-com.myaccess.library.utoronto.ca/articles/
767 s41593-018-0118-0, doi: 10.1038/s41593-018-0118-0.

768 **Tiesinga P**, Sejnowski TJ. Cortical enlightenment: are attentional gamma oscillations driven by ING
769 or PING? Neuron. 2009 Sep; 63(6):727–732. http://www.ncbi.nlm.nih.gov/pubmed/19778503, doi:
770 10.1016/j.neuron.2009.09.009.

771 **Tort ABL**, Kramer MA, Thorn C, Gibson DJ, Kubota Y, Graybiel AM, Kopell NJ. Dynamic cross-frequency cou-
772 plings of local field potential oscillations in rat striatum and hippocampus during performance of a T-maze
773 task. Proceedings of the National Academy of Sciences. 2008; 105(51):20517–20522. https://www.pnas.org/
774 content/105/51/20517, doi: 10.1073/pnas.0810524105.

775 **Traub RD**, Miles R, Buzsáki G. Computer simulation of carbachol-driven rhythmic population oscillations in the
776 CA3 region of the in vitro rat hippocampus. The Journal of physiology. 1992; 451:653–672.

777 **Whittington MA**, Traub RD, Kopell N, Ermentrout B, Buhl EH. Inhibition-based rhythms: experimental
778 and mathematical observations on network dynamics. International Journal of Psychophysiology: Official
779 Journal of the International Organization of Psychophysiology. 2000; 38(3):315–336. doi: 10.1016/s0167-
780 8760(00)00173-2.

781 **Wilson HR**, Cowan JD. Excitatory and Inhibitory Interactions in Localized Populations of Model Neurons. Bio-
782 physical Journal. 1972 Jan; 12(1):1–24. http://www.sciencedirect.com/science/article/pii/S0006349572860685,
783 doi: 10.1016/S0006-3495(72)86068-5.

784 **Wilson MA**, Varela C, Remondes M. Phase organization of network computations. Current Opinion in Neu-
785 robiology. 2015 Apr; 31:250–253. http://www.sciencedirect.com/science/article/pii/S0959438814002475, doi:
786 10.1016/j.conb.2014.12.011.

787 **Zhang X**, Zhong W, Brankačk J, Weyer SW, Müller UC, Tort ABL, Draguhn A. Impaired theta-gamma coupling
788 in APP-deficient mice. Scientific Reports. 2016 Feb; 6:21948. http://www.nature.com/articles/srep21948, doi:
789 10.1038/srep21948.

Acknowledgements

Author contributions statement

796 APC, JL, FKS conceived and designed research; APC, JL, SS, FKS performed research; APC, SS ana-
797 lyzed data; APC, JL, FKS interpreted results; All authors prepared figures and contributed to paper
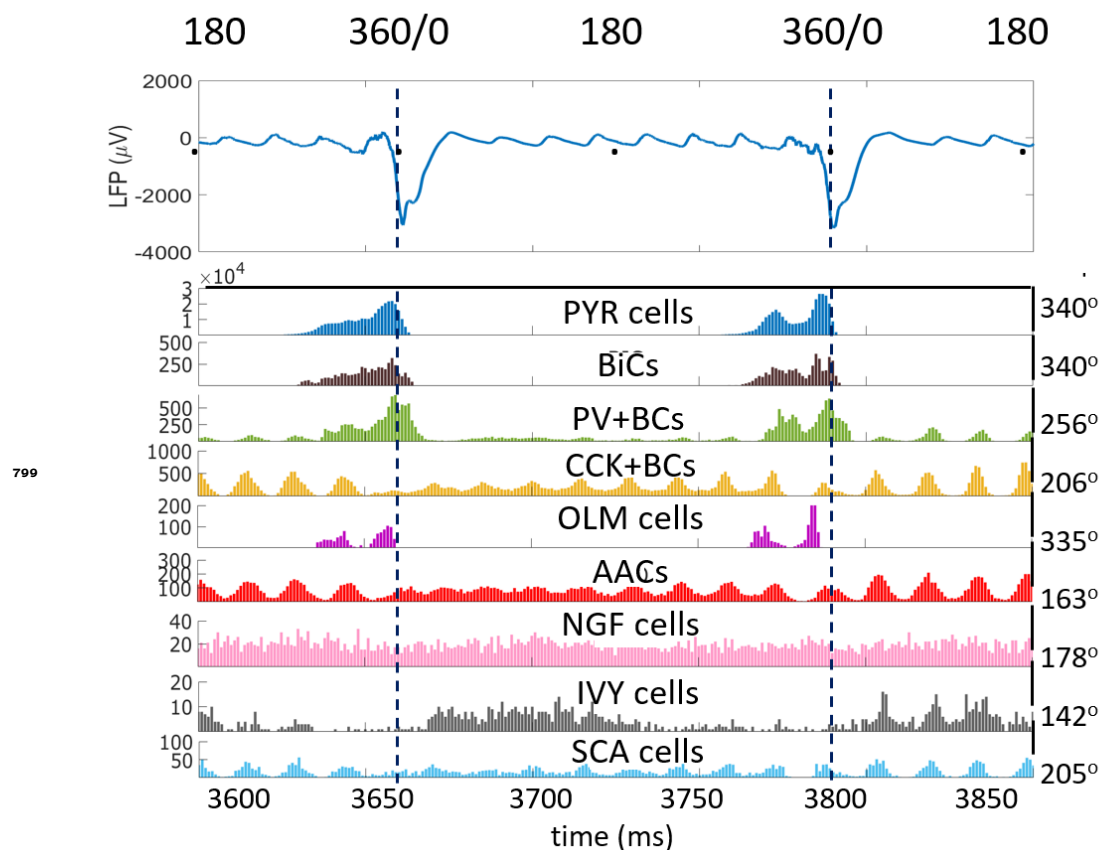798 draft writing. All authors reviewed the manuscript.

Figure 1—figure supplement 1. Theta phase preference detail.
LFP showing two theta cycles over 300ms with respective histogram plots of the eight inhibitory cell types and the PYR cells showing peak cellular firings relative to the LFP trough.
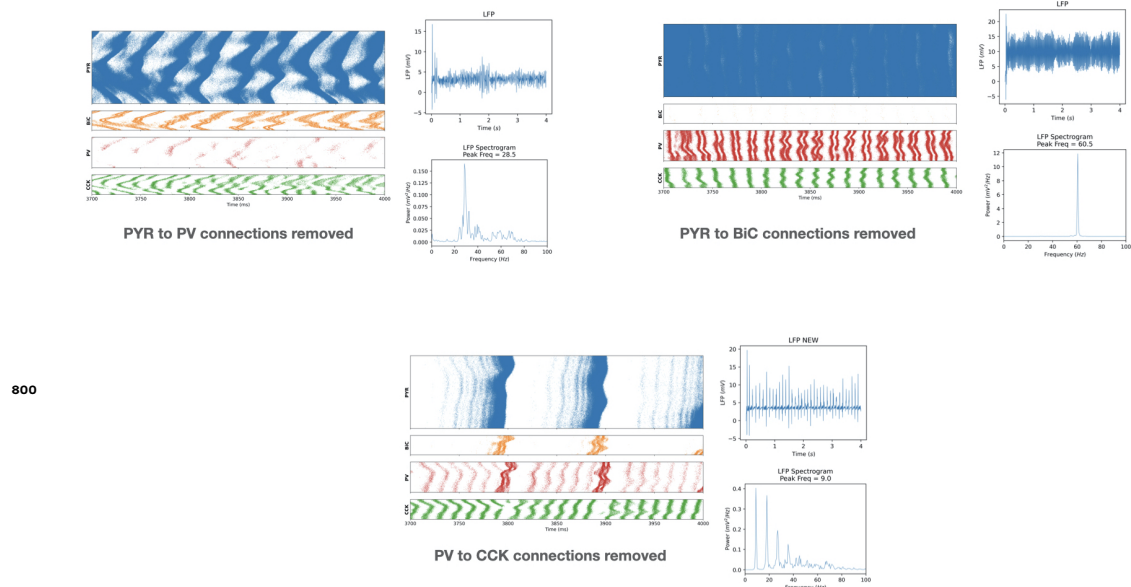
Figure 2—figure supplement 1. Additional connection removals in the detailed model.
A. Removing PYR cell to PV+BC connections. (i) Raster plots of cell firings (ii) unfiltered LFP, (iii) Welch's Periodogram of LFP. **B.** Removing PYR cell to BiC connections. (i) Raster plots of cell firings (ii) unfiltered LFP, (iii) Welch's Periodogram of LFP. **C.** Removing PV+BC to CCK+BC connections. (i) Raster plots of cell firings (ii) unfiltered LFP, (iii) Welch's Periodogram of LFP.
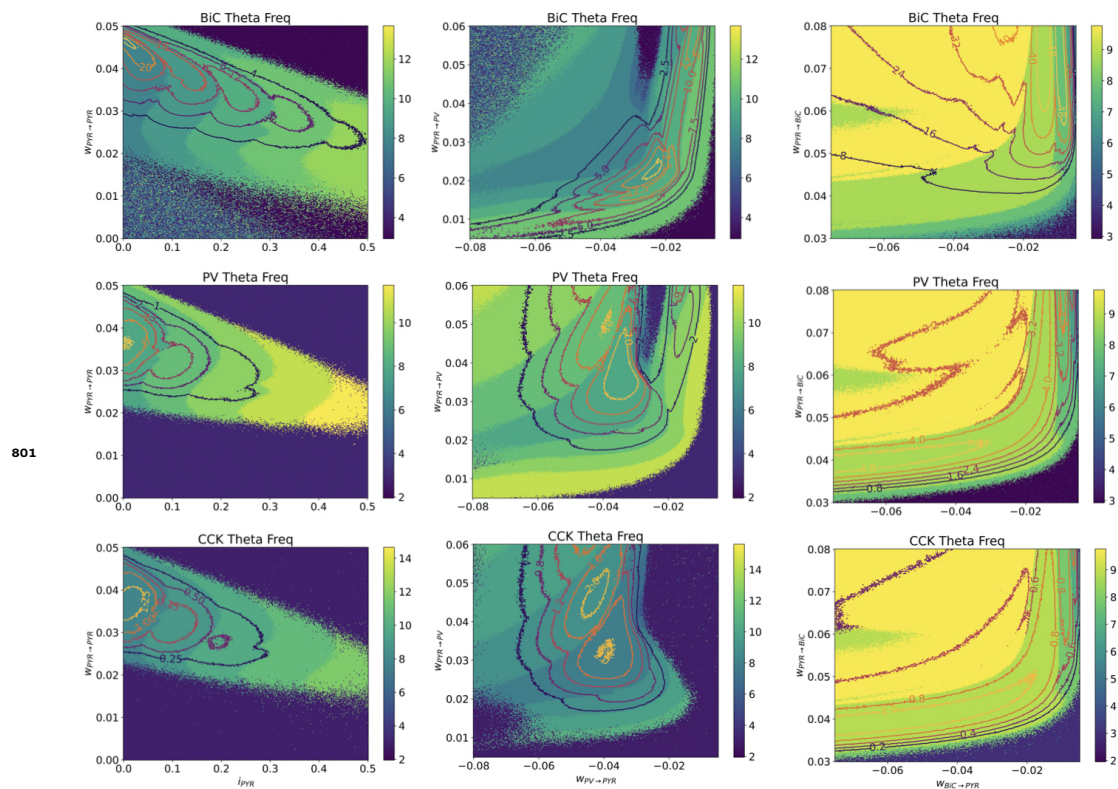

Figure 5—figure supplement 1. Theta frequency heat maps for other cell types.
BiC, PV+BC and CCK+BC cell types of the PRM for the same parameter sets in FIGURE 5 of main text are shown. Only PYR cell theta frequency heat maps are shown in the main text.
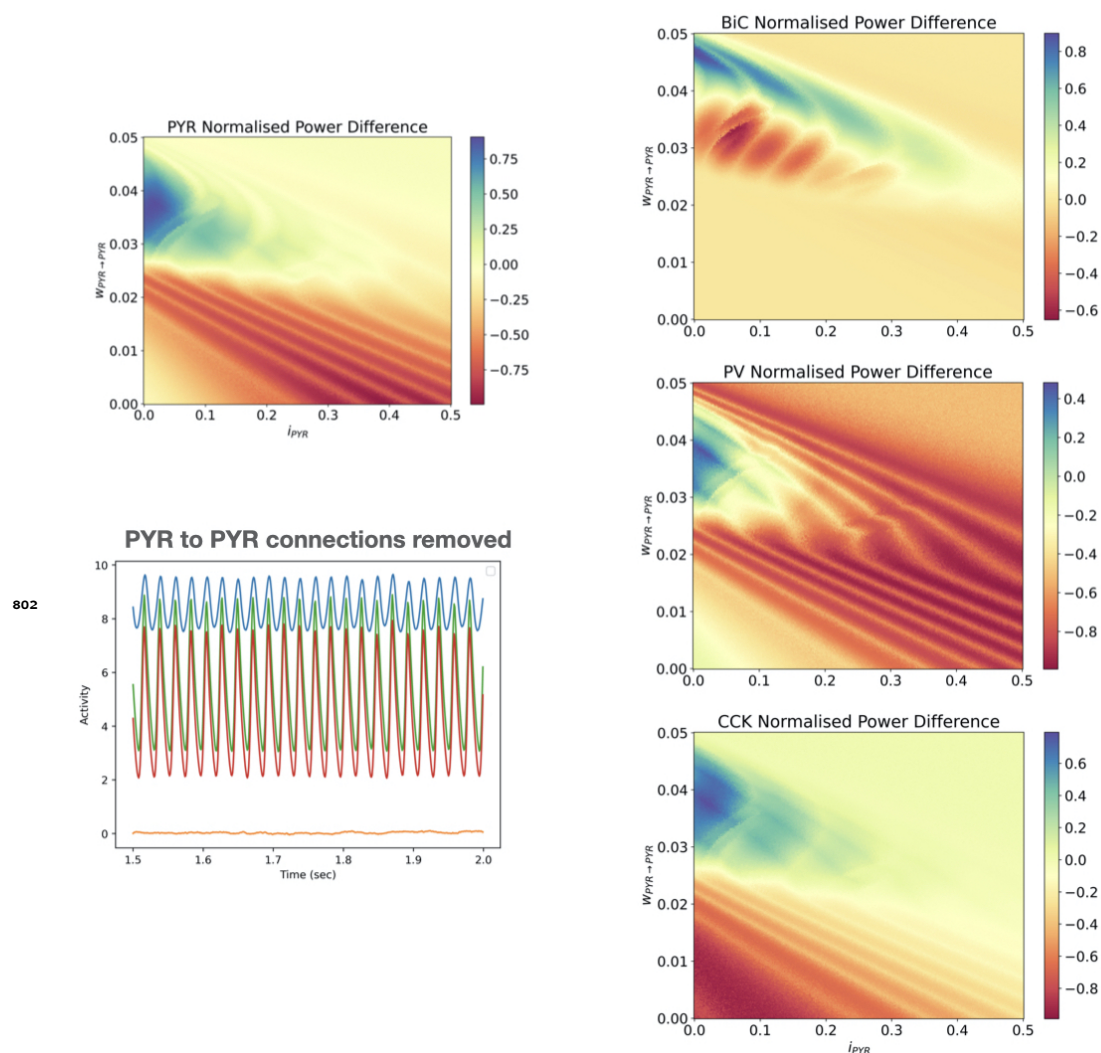
Figure 5—figure supplement 2. Difference heat maps.

Normalized theta and gamma power for $i_{pyr} - w_{pyr,pyr}$ are shown for all 4 cell types in difference heat maps (see Methods). Also shown is a plot of the output of cell activities with reference parameter values but when connections between PYR cells are removed ($w_{pyr,pyr} = 0$).

803

Figure 6—figure supplement 1. Additional difference heat maps.

BiC, PV+BC and CCK+BC cell types of the PRM for the parameter sets in FIGURE 6 of main text are shown. Only PYR cell heat maps are shown in the main text.

804

Figure 6—figure supplement 2. Difference heat maps for PYR-PV+BC and PYR-BiC couplings.

Difference heat maps are shown for $w_{BiC \to PYR} - w_{PYR \to BiC}$ (left) and $w_{PV \to PYR} - w_{PYR \to PV}$ (right) for PYR cell activity.